SPLEEN

Technical Summary of the instrumentation, measurement techniques and data reduction for the experimental test case SPLEEN C1

SPLEEN Identifier	SPLEEN-HSTC-DB-MeasurementTechniques
Author(s) and affiliation	S. Lavagnoli, G. Lopes, S. Simonassi, F.A.M. Torre (VKI)
Comments	Technical report that describes the instrumentation, measurement techniques, measurement locations, data processing and uncertainty of measurements performed on the SPLEEN C1 test case in the high-speed linear cascade S1/C of the von Karman Institute.

DOCUMENT HISTORY			
Version	**Date**	**Changed by**	**Reason of change**
1.0	30.10.2022	S. Lavagnoli	1st version

Contents

List of Figures

List of Tables

List of Symbols

A	cross-section area [m^2]
a	Sound speed [m s^{-1}]
C	Blade chord [m]
C_D	Drag coefficient [-]
E	Voltage [V]
F	Force [N]
g	pitch [m]
k_s	sand roughness [µm]
LE	Leading edge
LPT	Low-pressure turbine
l	Length [m]
$\dot{m}$	mass flow rate [kg s^{-1}]
ms	mesh size
M	Mach number [-]
P	pressure [Pa]
q	dynamic pressure [Pa]
PMFR	Purge mass flow rate [% of main flow]
R	Specific gas constant [J kg^{-1} K^{-1}]
r	Radius [m] (from the center of rotation)
Ra	centerline average roughness [µm]
Re	Reynolds number [-]
SMFR	Suction mass flow rate [% of main flow]
St	Strouhal number [-]
T	Temperature [K]
TE	Trailing edge
TI	Turbulence intensity [%]
U	Absolute velocity [m/s]
V	Mean velocity [m/s]
W	relative velocity [m/s]
WG	Wake Generator
Y	Pressure drop coefficient [-]

Greek Symbols

α	absolute incidence angle [deg]
β	relative incidence angle [deg]
	grid porosity [-]
δ	boundary layer thickness [mm]
γ	heat capacity ratio [-]
ϕ	diameter [mm]
Φ	flow coefficient [-]
µ	dynamic viscosity [kg m^{-1} s^{-1}]
ω	Rotational velocity [rad/s]
ρ	density [kg m^{-3}]
σ	solidity
θ	Ratio [%]

Subscripts

0	total conditions axis origin	r	rods
amb	Ambient	rad	radial
ax	Axial	s	static conditions
bar	WG bar	tang	tangential
BS	bar support	TG	turbulence grid
c	true chord	is	isentropic
in	inlet conditions (of the num. domain or cascade)	WG	wake generator
main	main flow	x	x-direction
out	cascade outlet	y	y-direction
purge	purge flow		

1 Introduction

The present report contains information on the experimental setup and hardware concerning cascade C1 (Chapter 2). In addition, the different types of instrumentation and placement are described (Chapter 2). In Chapter 3 the definition of operating conditions and establishing of the cascade operating point is discussed. Chapter 4 provides definitions for quantities reported in the database (losses, angles, etc.) and exposes different data reduction techniques employed throughout the project. Lastly, a thorough uncertainty analysis of the measured and derived quantities is presented in Chapter 5.

2 Experimental setup

The aim of this section is to present the linear cascade experimental setup. This section describes the cascade reference system used throughout the project and the measurement chain (sensors + data acquisition system).

2.1 The high-speed turbine cascade facility

The linear cascade measurements are conducted in the high-speed, low Reynolds facility S-1/C of the von Karman Institute. A sketch describing the facility is shown in Figure 2.1 This wind tunnel is a continuous closed-loop facility driven by a 615 kW 13 stages axial flow compressor. A heat exchanger allows controlling the flow temperature at near atmospheric condition. The mass flow is regulated via the adjustment of the compressor rotational speed and via a pressure regulation valve. A vacuum pump allows lowering the tunnel absolute pressure to below 8,000 Pascal. The cascade test section is in the first elbow of the wind tunnel loop (upper left elbow in Figure 2.1) following the diffuser. The cylindrical rear part of the diffuser is functioning as a settling chamber for the cascade test section. Wire meshes and honeycombs upstream of the test section ensure homogeneous flow conditions.

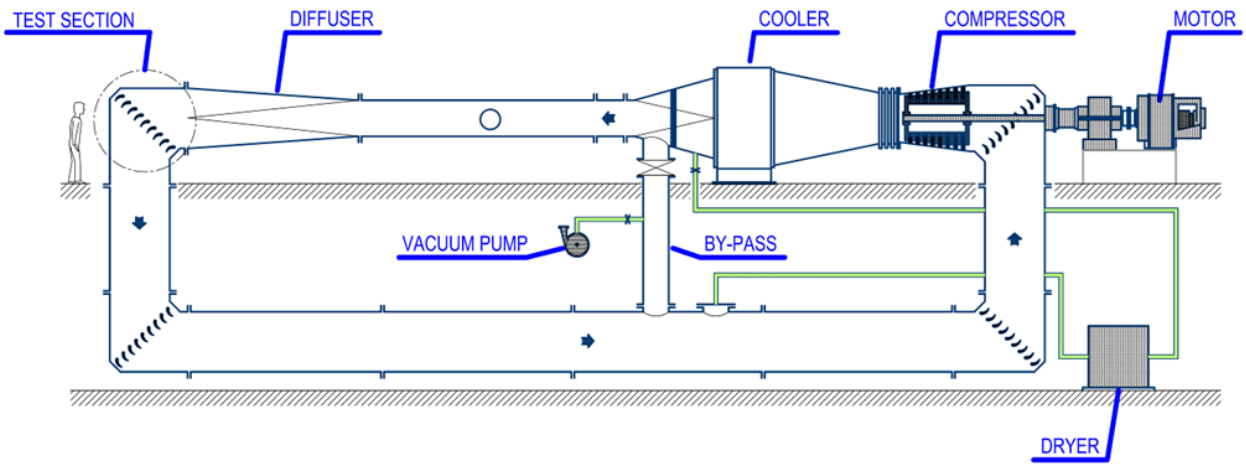

Figure 2.1: S-1/C wind tunnel.

A sketch and a picture of a typical LPT cascade model are shown in Figure 2.2. A bell mouth as well as vertical and lateral contractions provide the transition between the original circular parts of the wind tunnel and the cascade. The linear cascade ensemble is made up of several full blades (depending on the required pitch and chord length) plus two end-blocs at the cascade extremities. The cascade is mounted in between two large circular rotating sidewalls, which allow the fine adaptation of the inlet flow angle. Upstream passive grids vary the global free-stream turbulence intensity.

To simulate the blade-row interference effects due to wake-blade interactions, the test section is equipped with an upstream high-speed rotating bar system. The wake generator (WG) consists of a disc of 625 mm diameter equipped with cylindrical bars made of molybdenum at its periphery. The number and diameter of the bars as well as the rotational speed of the disk are adjustable to match a requested Strouhal number. The WG is driven by a 30 kW electric motor up to 3500 rpm which corresponds to a bar passing velocity at blade midspan of ~ 165 m/s that allows to establish engine-representative wake velocity triangles (i.e., flow coefficient).

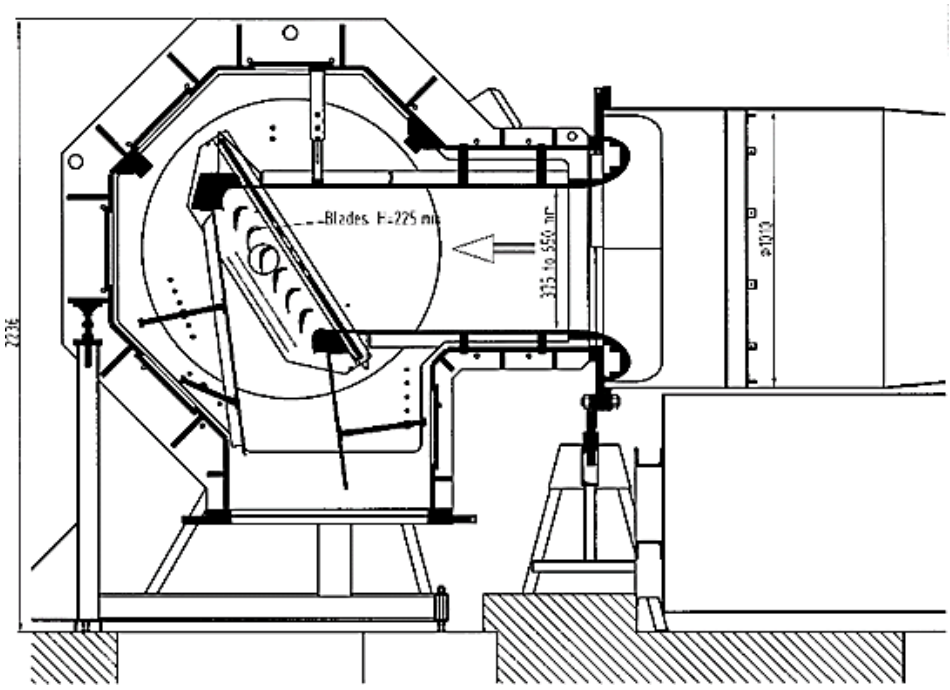

Figure 2.2: Sketch of typical S-1/C turbomachinery test section.

2.2 Instrumentation

2.2.1 Measurement planes

The cartesian reference system used throughout this study is presented in Figure 2.3. The origin point of the reference system sits at the intersection of the central blade LE with the cavity endwall (endwall at side of boundary layer lip and wake generator). The spanwise coordinate, z, increases from the origin towards the blade midpsan. The pitchwise coordinate, y, increases pressure side of the central blade to the suction side of the closest blade and the axial chordwise coordinate, x, increases from the origin towards the TE following a direction perpendicular to the plane containing the LE of all blades.

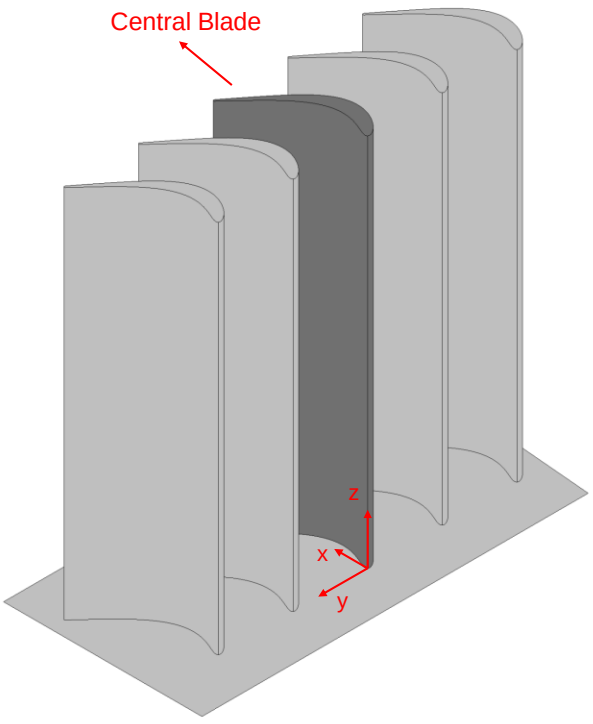

Figure 2.3: Measurement reference system.

Figure 2.4 illustrates the locations of the measurement planes across the cascade. Seven planes are selected at relevant axial stations:

- Plane ref. corresponds to the measurement plane of the reference total pressure and total temperature. The location of this plane depends on the rotation of the whole cascade. It sits at least 1 m upstream of the central blade LE.
- Plane 01 is aligned with the plane of rotation of the wake generator and it is located at x = $-1.12C_{ax}$.
- Plane 02 corresponds to the approximate exit location of the cavity slot. It is located at x = $-0.50C_{ax}$.
- Plane 03 is located at x = $0C_{ax}$ (Plane containing LE of all blades).
- Plane 04 is located at x = C_{ax} (Plane containing TE of all blades).
- Plane 05 and Plane 06 are parallel to Plane 04. Used to characterize the outlet flow field. Plane 05 and 06 are located at x = $1.25C_{ax}$ and x = $1.50C_{ax}$, respectively.

The location of the measurement planes as function of the blade axial chord is given in Table 2.1.

Table 2.1: Distance between measurement planes

Upstream of LE		**Blade**		**Downstream of TE**	
Plane 01	**Plane 02**	**Plane 03**	**Plane 04**	**Plane 05**	**Plane 06**
$-1.12C_{ax}$	$-0.50C_{ax}$	$0.00C_{ax}$	$1.00C_{ax}$	$1.25C_{ax}$	$1.50C_{ax}$

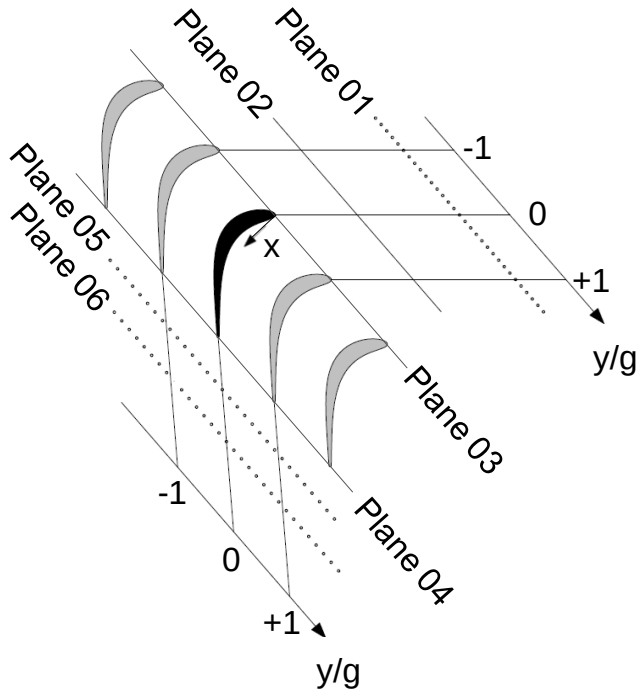

Figure 2.4: Location of measurement planes. Plane ref. not included.

One additional plane is defined $0.250C_{ax}$ downstream of Plane 06, named Plane 07. The purpose of this plane is to allow one additional location for the positioning of the probes used to characterize the flow field downstream of the cascade. No measurements are performed in this plane.

2.2.2 Cascade permanent instrumentation

Figure 2.5 shows the location of the permanent instrumentation in the test section. A description of each element is presented below.

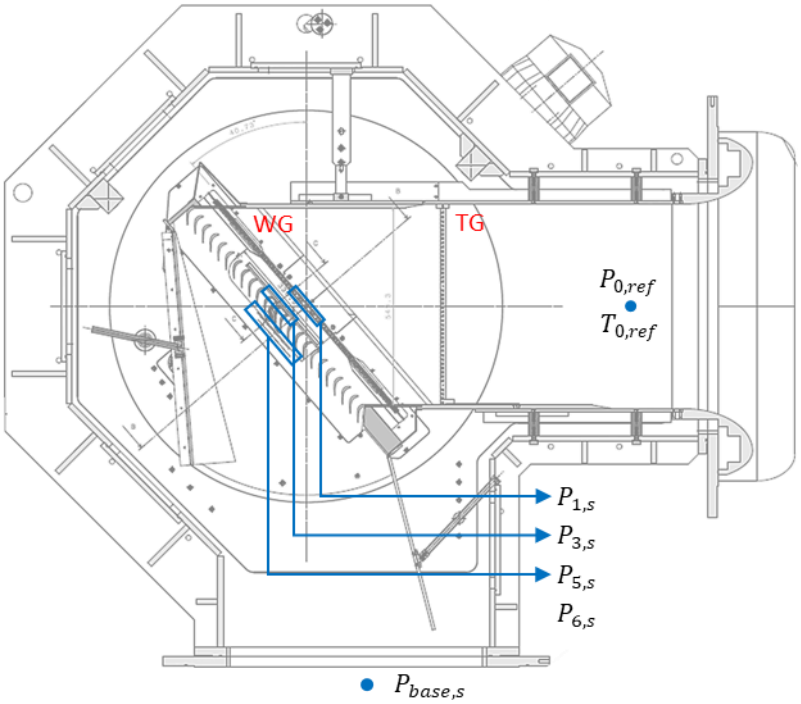

Figure 2.5: Cascade instrumentation for monitoring of rig/cascade operation

2.2.2.1 Reference quantities

Reference measurements of total pressure $P_{0,ref}$ and total temperature $T_{0,ref}$ are taken upstream of the turbulence grid. $P_{0,ref}$ is acquired by two pitot tubes placed in the section upstream the cascade at different height and depth. The upper one is at half-height of the diffuser, and the head of the probe is at a third of the width from the sidewall, while the lower one is placed at third of the height from the bottom of the diffuser, with the head placed at mid-width of the channel. A figure showing the pitot tubes location is presented in Figure 2.6. This double measurement allows to verify no spanwise pressure gradient is present upstream of the turbulence grid. When the turbulence grid is installed before the cascade, a total pressure drop is introduced. Since the probe is located upstream of the grid, the real total pressure at the cascade inlet cannot be directly measured and must be thoroughly characterized. The procedure is presented in section 2.2.2.6.

Figure 2.6: Location of the pitot tubes at the entrance of the test section.

$T_{0,ref}$ is measured using a K-type bare thermocouple. The total temperature probe is located slightly upstream of the total pressure probes, in a low velocity region, to ensure a temperature recovery factor of unity.

2.2.2.2 Plane 01 - Inlet static pressure (pneumatic pressure taps)

The inlet static pressure is monitored by time-averaged pneumatic pressure taps along the upper endwall in the same plane as the WG. 31 pneumatic static pressure taps with diameter of 1.00 mm are equally distributed (3.30 mm between taps) in the pitchwise direction, covering the length of three pitches (with the central tap aligned with the LE of the central blade).

2.2.2.3 Plane 03 – LE Inlet static pressure (pneumatic pressure taps)

The inlet static pressure at the location of the leading edge is monitored by means of time-averaged pneumatic pressure taps along the upper endwall at Plane 03. Fourteen equally spaced static pressure taps with diameter of 1.00 mm are distributed in the pitchwise direction, covering two pitches. The taps are part of the assembly used with the smooth central blade, therefore the taps at Plane 03 are installed only during the measurements with this specific blade.

2.2.2.4 Plane 05 and Plane 06 - Outlet static pressure (pneumatic pressure taps)

Static pressure taps are distributed in the pitchwise direction in Plane 05 and Plane 06, covering four pitches. A total of 31 equally spaced pneumatic taps with diameter of 1.00 mm are distributed (4.40 mm spacing between each tap) along four cascade pitches where the central pneumatic tap is aligned with the central blade TE.

2.2.2.5 Cascade base pressure

With the aim to control the long-term stability of cascade operating conditions during probe measurements, the static pressure in the wind tunnel far downstream of the test section is monitored. This solution is necessary to correctly regulate the flow conditions, avoiding interferences because of the traversing probes on the static pressure measured by the cascade fixed taps used to compute the instantaneous operating conditions. A single pressure tap is used for this purpose following a careful in-situ calibration when no probes are immersed in the flow (see section 3.5).

2.2.2.6 Wake generator speed and position

The angular position and velocity of the wake generator is assessed using a photocell combined with a toothed wheel mounded on the wake generator shaft. The toothed wheel presents 29 equally spaced teeth and one smaller tooth. The signal of the photodiode is 9 V when the diode light passes in the empty spaces between the teeth and 0 V when the space between the photocell is blocked by the teeth. During the wake generator assembling, the wake generator bars were phased with respect to the cascade central blade leading edge. The processes required to align the bar number 1 with the central blade leading edge (following the inlet metal angle) while positioning the second edge of the small tooth (second in the direction of rotation) in correspondence of the location where the photo-diode signal rises to 9 V. A schematic view of the bar alignment and a picture taken during the process are reported in Figure 2.7. An example of the photodiode signal emitted by the photodiode is shown in Figure 2.8 compared with the wheel position.

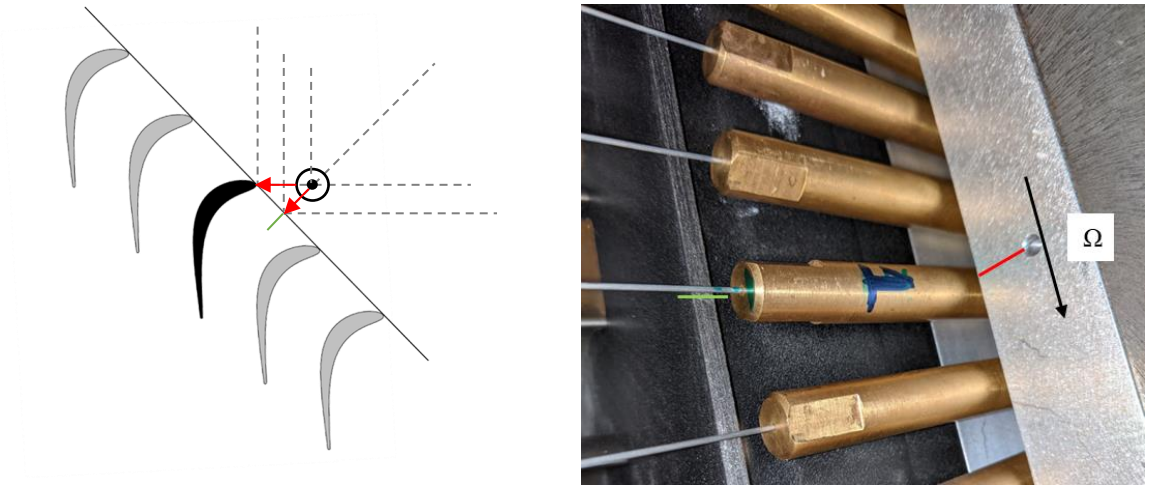

Figure 2.7: Phasing of the wake generator bars with the central blade leading edge. The sketch on the left side shows the WG bar aligned with the central airfoil LE along the projection of the airfoil metal angle (bar phase = 0.0)

The green line in the photo in Figure 2.7 represents the projection of the central blade LE used to align the bar. This procedure allows to determine the instantaneous position of the WG bars with respect to the cascade central blade leading edge. The relative position of each bar with respect to the central airfoil leading edge is expressed in non-dimensional terms using the bar phase. The zero phase corresponds to the time when the bar center is aligned with the leading edge of the central airfoil along the direction defined by the airfoil metal angle, the phase equal to 1 corresponds to the time when the next bar center is aligned to the same airfoil leading edge, i.e. the wake generator bars have traversed one full bar pitch.

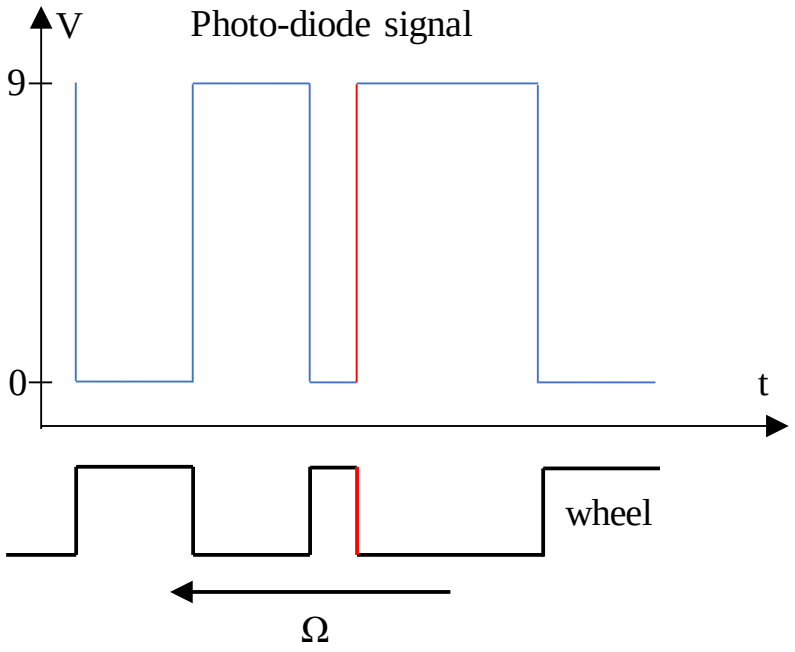

Figure 2.8: Photodiode signal and wake generator toothed wheel position. Second edge of the short tooth in the direction of rotation is the reference for the bar #1 aligned with the central blade LE (corresponding to a bar phase of 0.0).

2.2.3 Probes

A list of probes used during the experimental campaign is reported in Table 2.2.

Table 2.2: Probes of SPLEEN C1 experimental campaign

Types	SPLEEN nomenclature	Measurement scope
Preston boundary layer probe	P-PNEU-BL-01	Boundary layer profile and status (integral parameters)
Thermocouple type-K probe	P-ThermoK-01	Inlet Temperature profile
Single hot-wire measurement (// to the endwall)	P-HW-01	Inlet free-stream turbulence intensity + Boundary layer profile and status
Single hot wire measurement (// to the cascade spanwise direction)	P-HW-02	Bar and blade wake turbulence intensity and length scales
Fast response virtual 4h probe	P-FR-4H-01	Unsteadiness of inlet and outlet flow conditions (P0, pitch and yaw angle)
Pneumatic virtual 4h probe	P-PNEU-4H-01	Inlet and outlet flow conditions (P0, pitch and yaw angle)
Miniature pneumatic 5h probe (Cobra-shaped) upstream measurements	P-PNEU-C5H-01	Inlet pitch and yaw angle (P0, pitch and yaw angle)
Miniature pneumatic 5h probe (L-shaped) downstream measurements	P-PNEU-L5H-01	Outlet flow conditions (P0, pitch and yaw angle)

The probes are traversed in the test section using the probe carriage system shown in Figure 2.9. Motor #1 provides the pitch-wise motion, motor #2 moves the probe in span-wise direction, while the probe rotation is driven by motor #3. The accuracies of setting a probe pitchwise and spanwise location, as well as the yaw angle are $\pm 0.1\ mm$ and ± 0.1 deg, respectively.

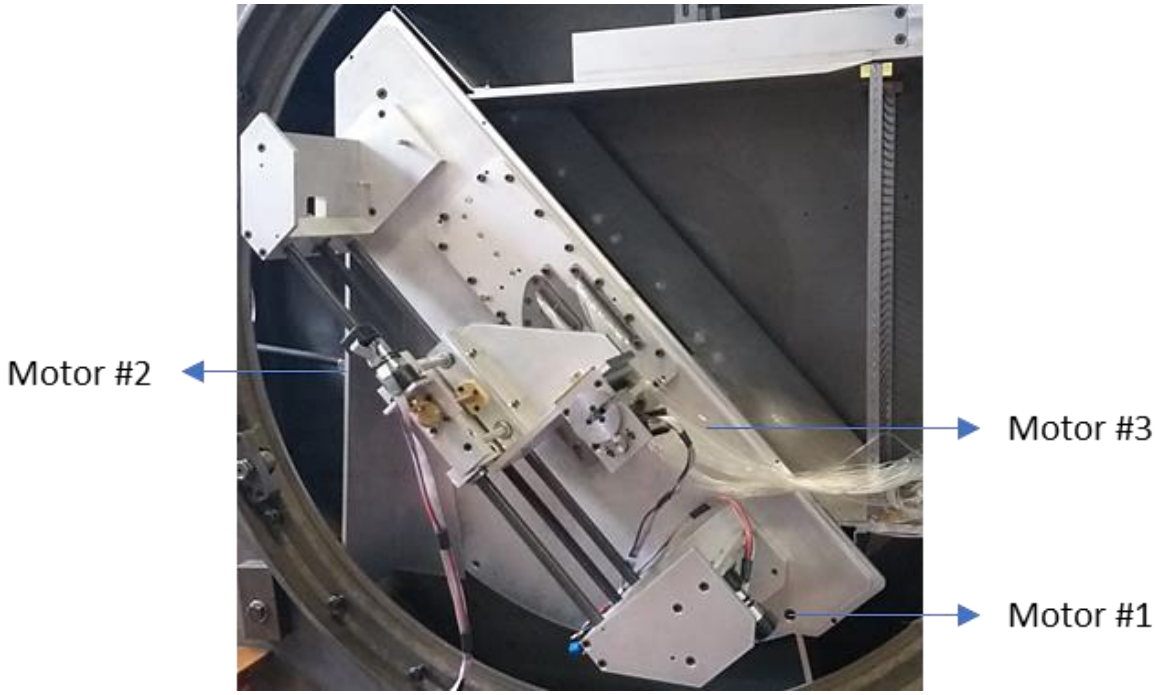

Figure 2.9: Probe traversing unit mounted on the SPLEEN test section.

2.2.3.1 Preston boundary layer probe

The probe is traversed in Plane 01. A picture of the probe and the dimensions of its head is presented in Figure 2.10.

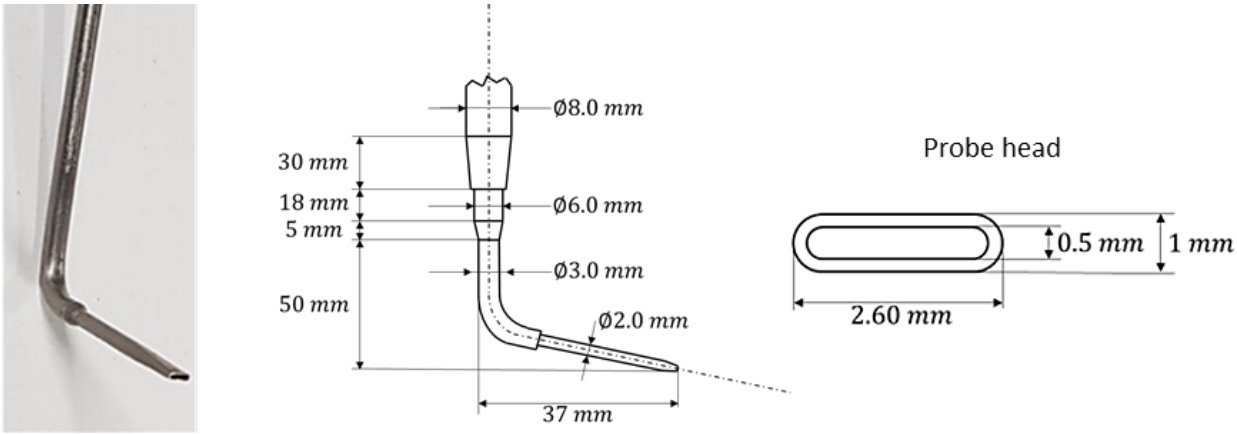

Figure 2.10: Preston boundary layer probe P-PNEU-BL-01.

2.2.3.2 *Thermocouple K probe*

The probe is traversed in plane 01. A picture of the probe and the dimensions of its head is presented in Figure 2.11. The wire diameter is ϕ_{wire} = 50 µm.

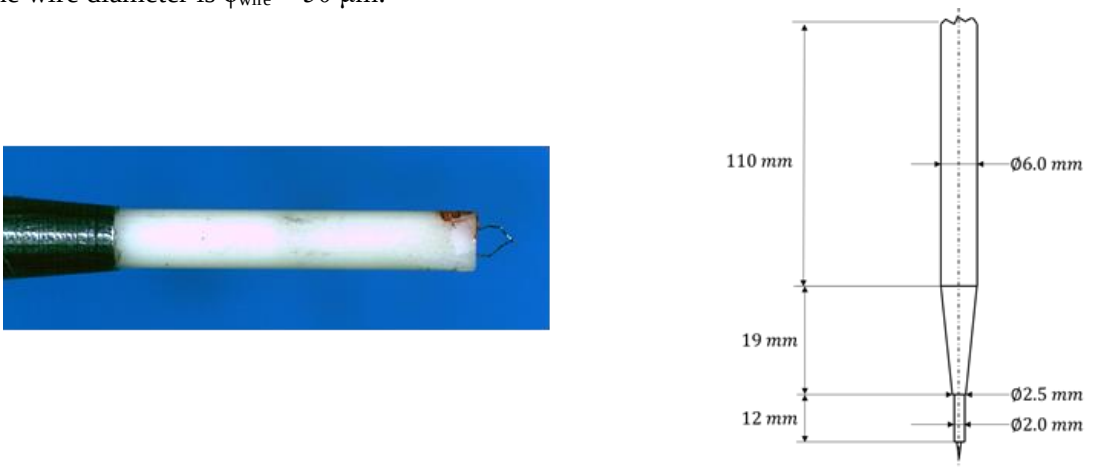

Figure 2.11: Thermocouple K probe P-ThermoK-01.

2.2.3.3 *Hot-wire measurements*

Two probes are used for the HW measurements at the inlet of the test section. The difference between the probes is in the wire orientation. The first probe presents a 9 µm wire perpendicular to the probe stem axis, i.e., parallel to the cascade endwall when the probe is in the test section. This probe is used for the characterization of the inlet free-stream turbulence intensity and of the boundary layer profile and status. A picture of the probe and its dimensions is presented in Figure 2.12.

Figure 2.12: P-HW-01.

The second HW probe is used for measurements of wake generator bars and blade wake turbulence intensity and length scales. To achieve this goal, the wire is parallel to the probe axis. The probe geometry is shown in Figure 2.13.

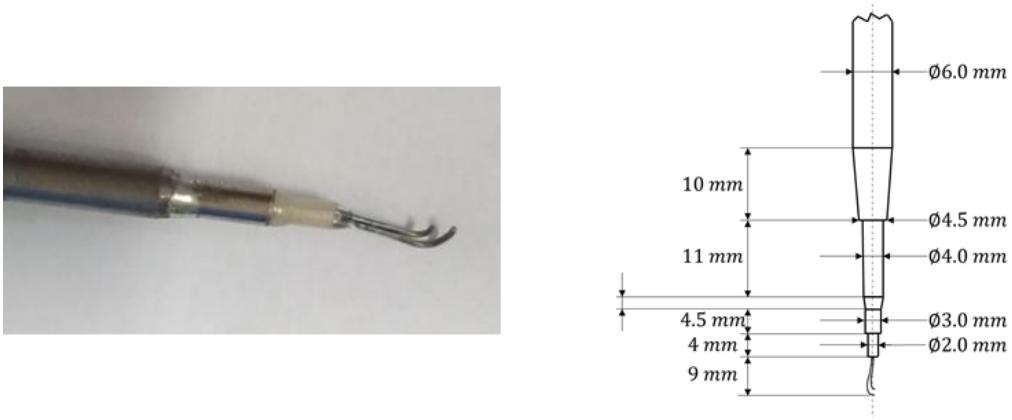

Figure 2.13: P-HW-02.

2.2.3.4 Virtual four holes probes

A pneumatic two-holes probe meant to be used as a virtual four holes probe was built and calibrated. The probe head can be seen in Figure 2.14. The probe is used to survey the inlet and outlet flow conditions (P0, pitch and yaw angle).

.

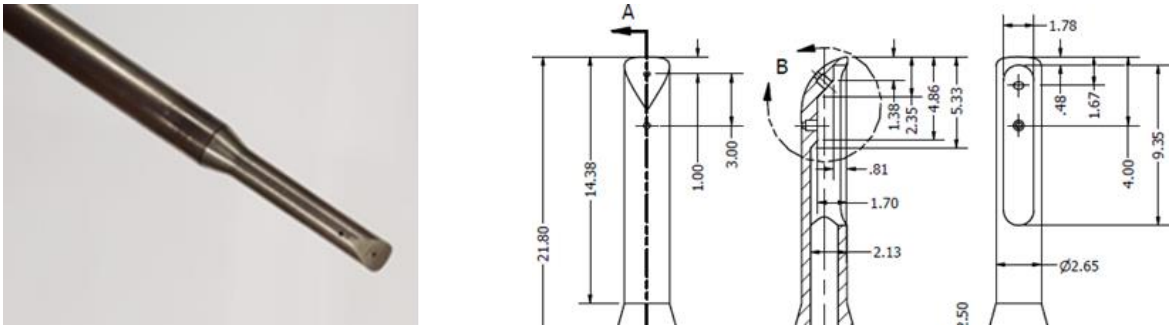

Figure 2.14: Pneumatic virtual 4h probe P-PNEU-4H-01.

The fast response virtual four holes probe is identical to the pneumatic twin. A sketch showing the internal of the probe head s presented in Figure 2.15. The spanwise distance between the two measuring pressure ports is 3.00 mm.

The probe is instrumented with two low-range piezo-resistive transducers Kulite LQ-062-5A (5psi A – 34.4 kPa A). Details of the Kulites are reported in 2.2.6.4. The yaw sensitive sensor is named *"Kulite 1"*, while the pitch sensitive one is named *"Kulite 2"*. Because of the low range sensors, the calibration of this probe was performed by means of the twin pneumatic probe presented above. the calibration obtained with P-PNEU-4H-01 performed under atmospheric conditions will be applied to the P-FR-V4H-01 under the wind tunnel operating conditions. An in-situ angular calibration in yaw angle is also performed for both pneumatic and fast-response version of the virtual 4-hole probes. The in-situ calibrations are compared against the aerodynamic calibration performed at atmospheric density conditions to verify the insurgence of Reynolds effects that limit the range of applicability of the aerodynamic calibration at atmospheric conditions (i.e., at high Reynolds).

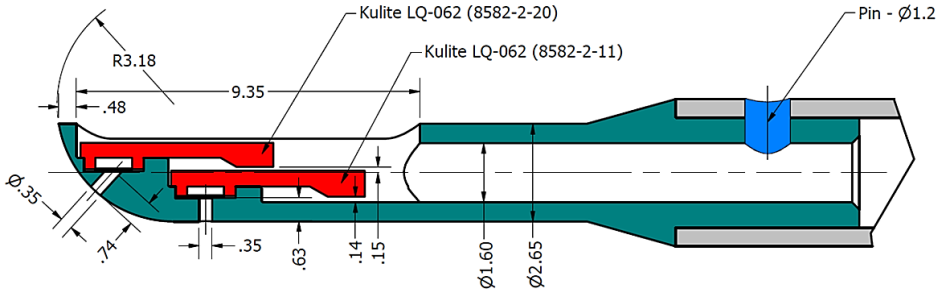

Figure 2.15: Fast response virtual 4h probe P-FR-4H-01.

2.2.3.5 *Pneumatic five holes probes*

Two five holes probes are used to characterize the cascade inlet and outlet flow field. A cobra shaped five holes probe is used to survey the flow in the inlet Plane 02. The cobra shape allows the measurement location to be in the same plane of the probe insertion slot. Figure 2.16 shows a picture of the probe head and a sketch reporting the main dimensions of the probe.

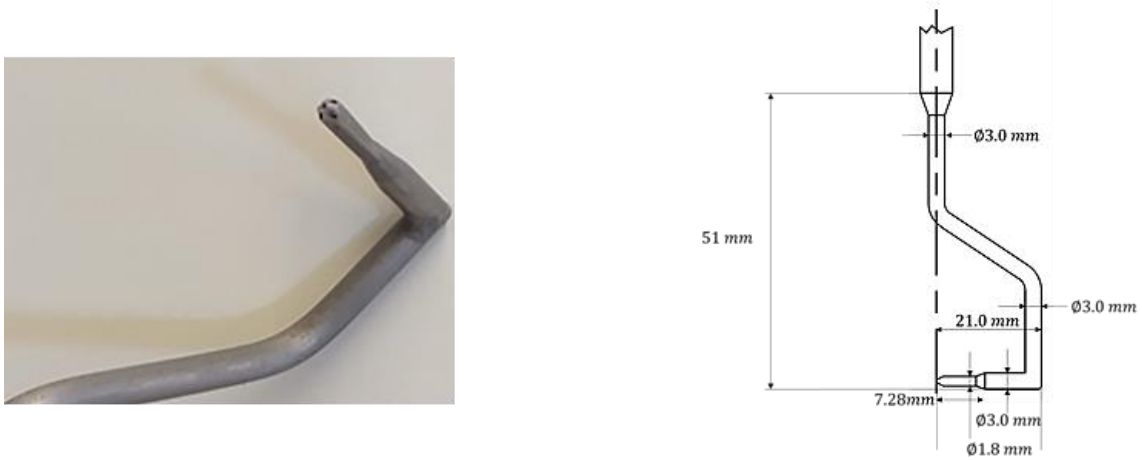

Figure 2.16: Cobra five holes probe P-PNEU-C5HP-01

The flow field downstream of the cascade is sampled by means of a miniaturized L-shaped five holes probe. The probe head is 2.2 mm. The L-shape allows the measuring head to be located upstream of the probe stem, reducing the impact of the probe on the cascade flow field. A photo of the probe head and the corresponding dimensions are shown in Figure 2.17.

Figure 2.17: L-shaped five holes probe P-PNEU-L5HP-01

The L-shape design allows the probe to be mounted in two different locations and sample the flow field in both Plane 05 and Plane 06. To measure in Plane 05, the probe stem is mounted in the slot located in Plane 06 while the additional slot in Plane 07 is used to locate the probe head in Plane 06. One important consideration is that, given the geometry of the cascade, the mounting angle of the probe that allows the head to be located exactly in the measurement plane is only one: 85.3 deg with respect to the horizontal. This angle is valid given the 40.73 deg rotation of the cascade. When the cascade is rotated to accommodate for the effect of the wake generator, the new angle of the downstream L-shaped probe is 79.1 deg. A sketch presenting the angular positioning of the L-shaped five holes probe is reported in Figure 2.18.

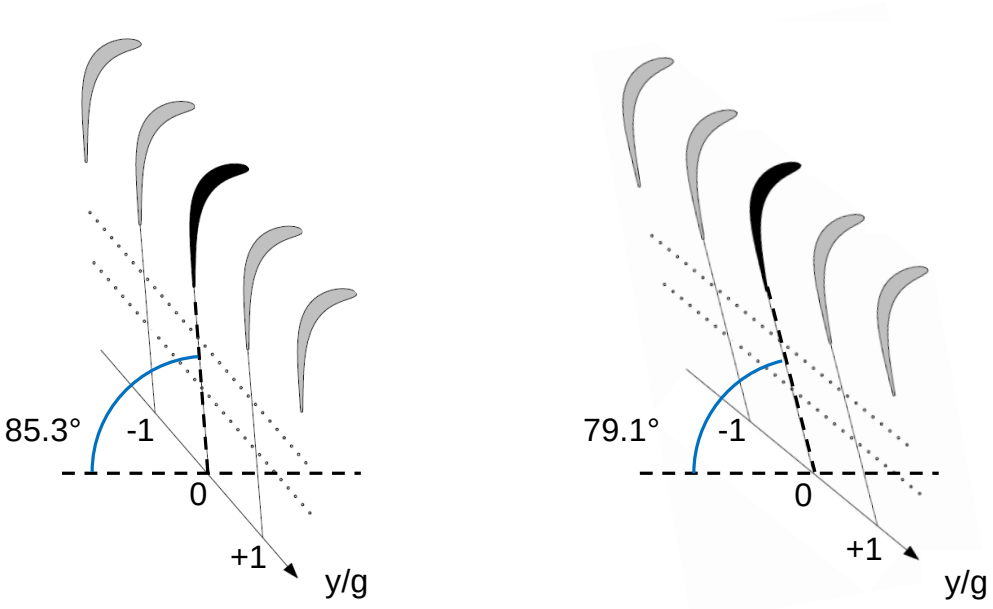

Figure 2.18: Angular positioning of the L-shaped five holes probe in the downstream planes.

2.2.4 Blade surface measurements

The characterization of the blade aerodynamics is carried out by means of several instrumented traversable blades.

The concept of the central sliding instrumented blade allows the movement along the spanwise direction to translate the array of sensors, keeping a dense spatial resolution. The design of the actuation system permits the sensors to be translated from the endwall to mid-span. Figure 2.20 and Figure 2.21 show the concept, the design, and the mounted carriage system. A servomotor actuates the blade. The traverse carriage system allows to achieve a linear position accuracy of $\pm 0.1\ mm$ and angular precision of $\pm 0.1°$.

A clearance of 0.05 mm is established between the 3D printed endwall and the sliding blade. Such gap is necessary to avoid interference between the instrumented blade and the fixed endwall during operation, while the small size of the clearance limits the leakages from high to low pressure regions to negligible levels. A schematic representation of the clearance is displayed in Figure 2.19.

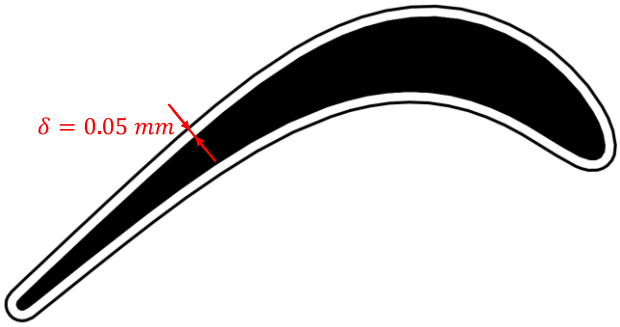

Figure 2.19: Schematic figure highlighting clearance between blade and 3D printed endwall

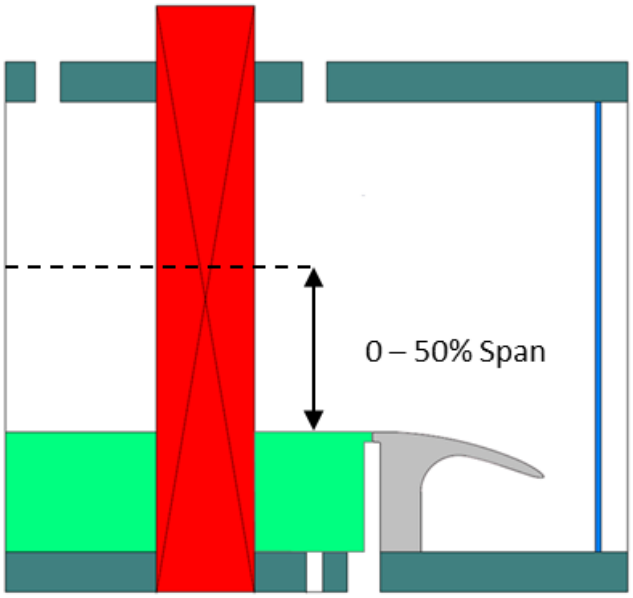

Figure 2.20: Sliding blade concept.

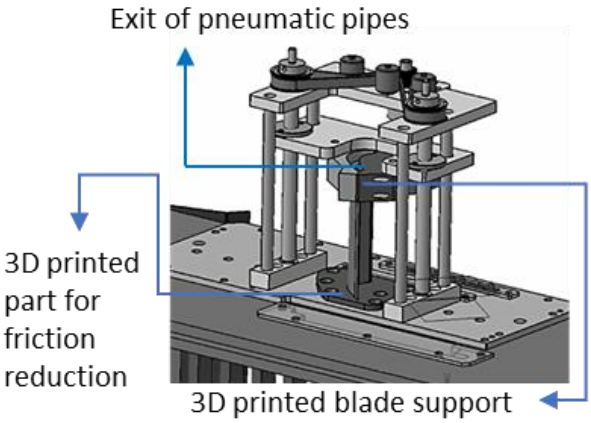

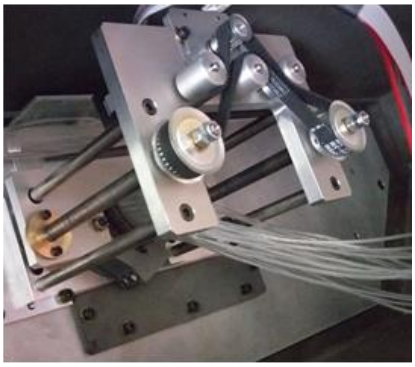

Figure 2.21: Sliding blade carriage system

2.2.4.1 *Instrumented Blade with suction side pressure taps (B-PNEU-SS)*

Figure 2.22 displays the position and the geometry of the pneumatic taps on the suction side of the SPLEEN C1 airfoil as well as the dimensions and the characteristics of the groove for the tubing that routes out the pressure information. Note all grooves and tubing are carefully polished after installation to resume a smooth continuous surface over the airfoil.

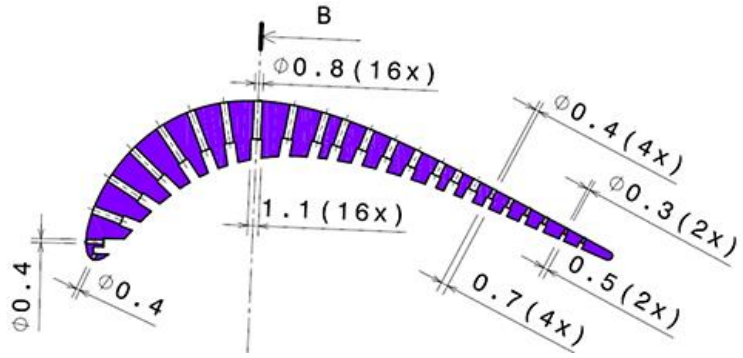

Figure 2.22: B-PNEU-SS pneumatic taps positioning and dimensions

2.2.4.2 *Instrumented Blade with suction side fast-response sensors (B-FR-SS)*

The location of the fast response pressure transducers on the SPLEEN C1 blade as well as the dimensions and the characteristics of the mounting grooves are depicted in Figure 2.23. The blade is equipped with 7 Kulites of the series LQ-062-5A.

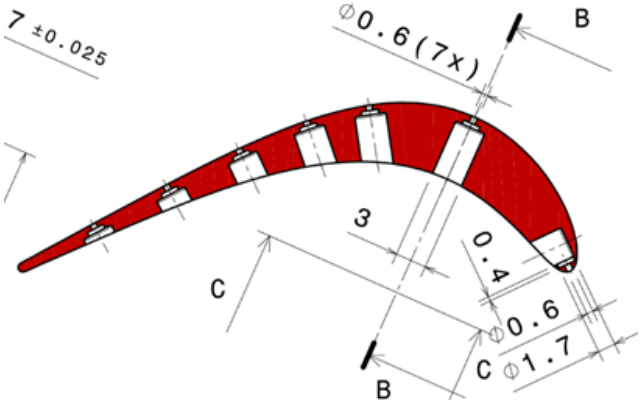

Figure 2.23: B-FR-SS fast response taps location and dimensions

2.2.4.3 *Instrumented Blade with pressure side pressure taps and fast-response sensor (B-PNEU-FR-PS)*

One single blade houses both pneumatic taps and one fast response pressure transducer on the blade pressure side. The positioning for the B-PNEU-FR-PS blade as well as the dimensions and the characteristic of the groove is presented in Figure 2.24. The blade is equipped with 1 Kulite of the series LQ-062-5A.

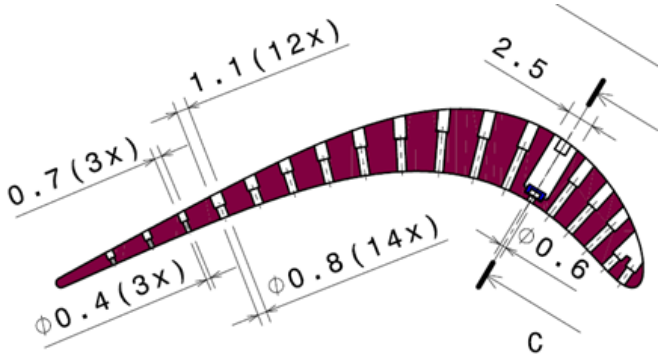

Figure 2.24: B-PNEU-FR-PS fast response and pneumatic taps location and dimensions

2.2.4.4 *Instrumented Blade hot-film gauges (B-HF)*

A schematic view of the location of the hot-film gauges and lead dimensions, as well as their location along the blade surface is depicted in Figure 2.25. All the sensors have the same dimensions (width of 0.1016 mm, thickness of 0.0002 mm and length of 1.4478 mm). The sensor leads have the same geometry as well (width of 0.60 mm, thickness of 0.0127 mm, length of 215 mm, gap between adjacent leads of 0.40 mm). The sensor interspacing is 2 mm. Figure 2.26 shows a view of the B-HF mounted in the test section.

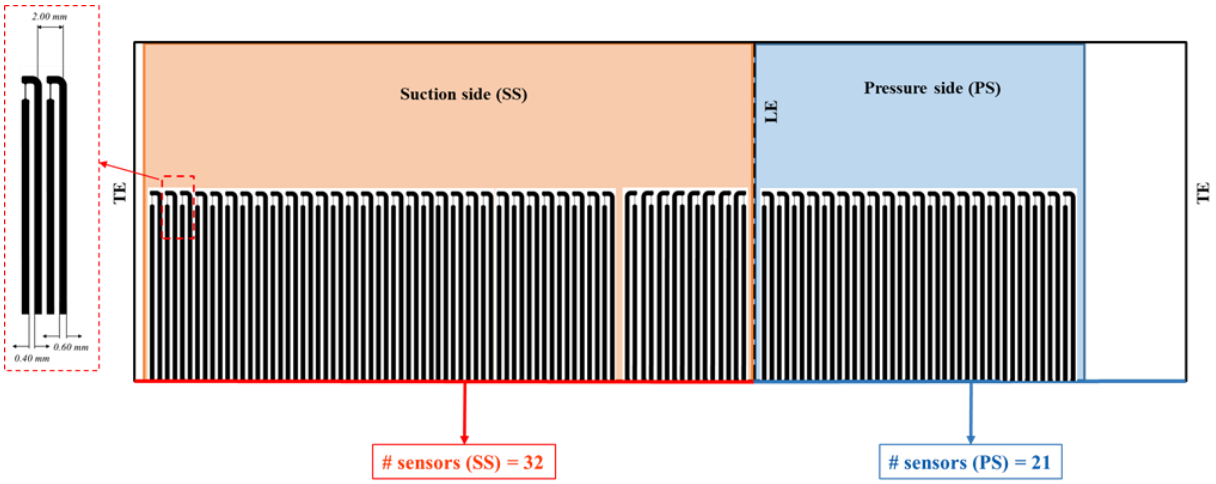

Figure 2.25: Schematic representation of the hot-film gauges positioning and lead dimensions.

Figure 2.26: Blade instrumented with fast-response hot-film sensors mounted in the SPLEEN cascade.

2.2.5 Endwall measurements

The two endwall (EW) passages adjacent to the central blade can be instrumented with pneumatic and fast-response pressure taps as well as surface mounted hot-films. The geometry of the inserts is shown in Figure 2.27. Two smooth inserts with no instrumentation are used during the probe and blade measurements to avoid possible intrusiveness effects of the instrumented EW inserts on the secondary flow structures (Figure 2.27 (b)).

Two pressure endwall inserts with a total number of 66 pneumatic taps with diameter of 1.00 mm and 8 fast-response taps with diameter of 0.80 mm (Figure 2.27 (b)) are used to resolve the steady and unsteady wall pressure. Similar to the design of blade surface mounted hot-films, the maximization of sensors on the endwall was attempted (Figure 2.27 (c)).

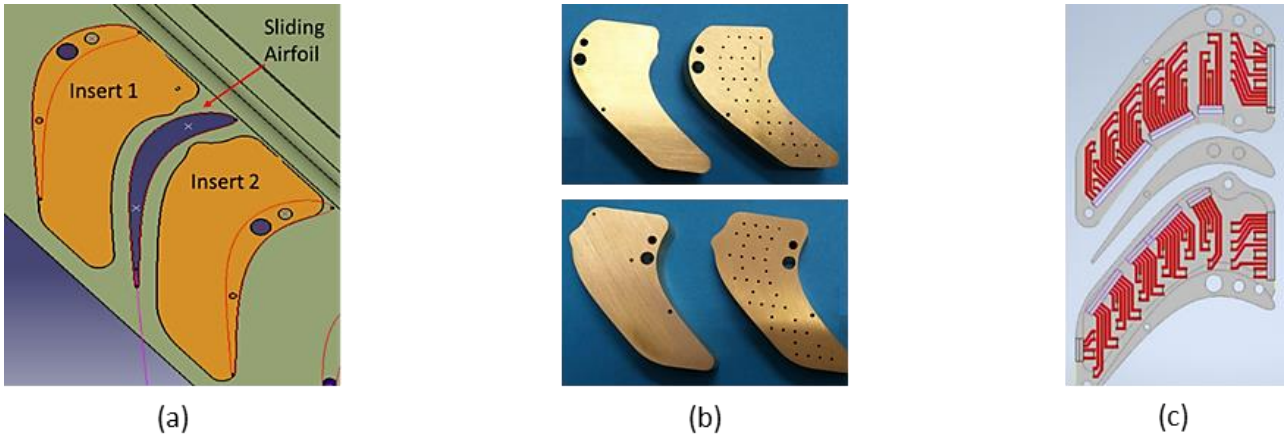

Figure 2.27: Endwall inserts geometry (a), smooth endwall inserts and pneumatic and FR pressure taps inserts (b) and surface mounted hot-film inserts (c).

2.2.5.1 Smooth endwall inserts

A picture showing the integration of the smooth inserts in the SPLEEN cascade can be seen in Figure 2.28.

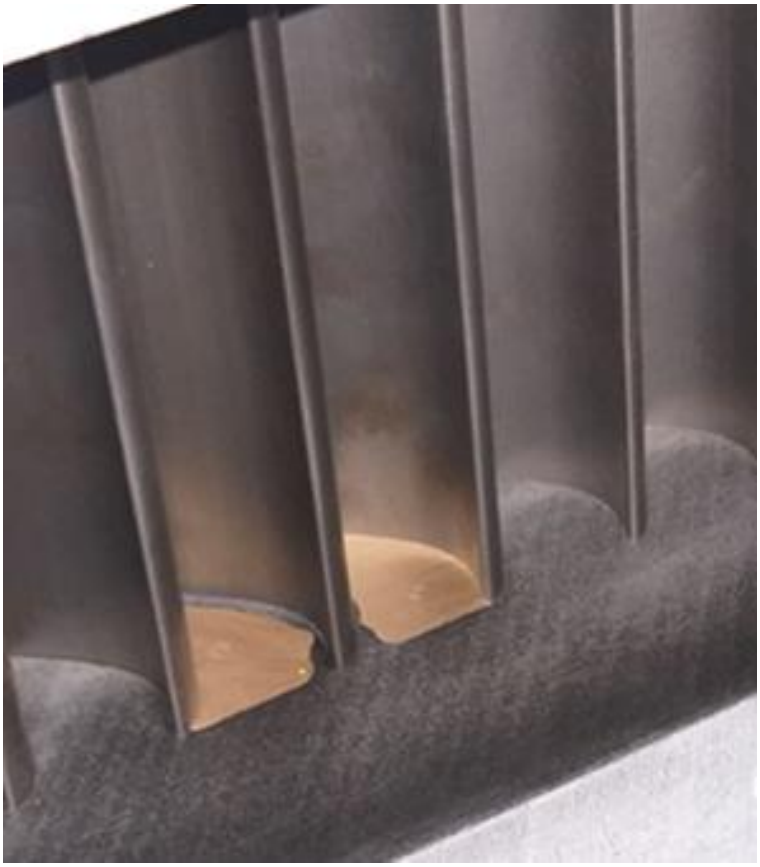

Figure 2.28: Integration of the smooth inserts in the SPLEEN cascade.

2.2.5.2 *Pressure endwall inserts*

The finalized instrumented endwall inserts with pneumatic and fast response taps are shown in Figure 2.29. The inserts located on SS and PS passage of the central blade are named “Insert 1” and “Insert 2” respectively. Insert 1, located in the upper passage, including the SS of the central blade contains 6 Kulites sensors and 30 pneumatic taps. The insert on the lower passage, which includes the central blade PS, has 36 pneumatic taps and 2 Kulites. The Kulites sensors used for this application are of the series XCQ-062-5A. All pneumatic and fast-response taps have a diameter of 1.00 mm and 0.80 mm, respectively.

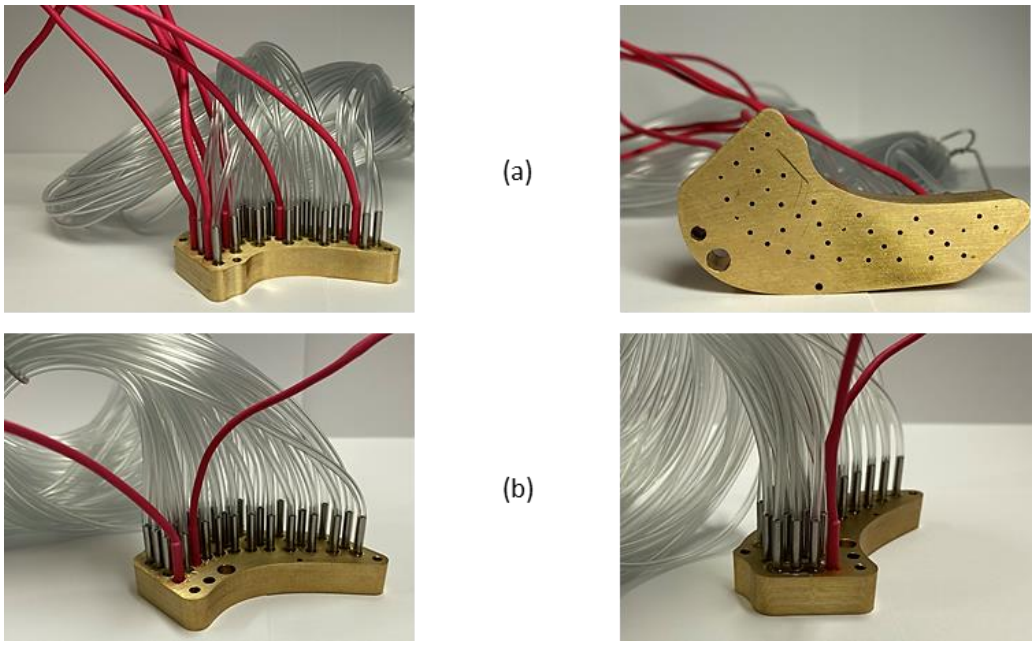

Figure 2.29: Instrumented endwall inserts. Insert 1: 30 pneumatic taps and 6 fast response sensors (a). Insert 2: 36 pneumatic taps and 2 fast response sensors (b).

Considering the periodicity of the two passages around the central blade, the data acquired with the pneumatic and fast response taps are merged in the post-processing phase. A sketch of the two separate inserts and the resulting virtual insert with the combined sensors is shown in Figure 2.30.

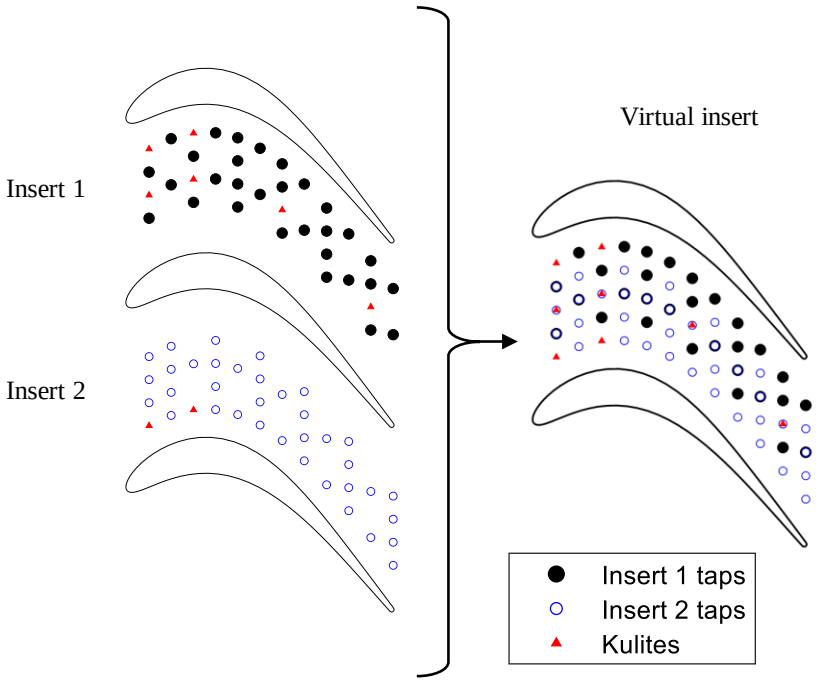

Figure 2.30: Endwall Inserts 1 and 2 and generation of Virtual insert.

2.2.5.3 *Hot-film endwall inserts*

Endwalls around the central blade are equipped with 48 high-response hot-film gauges to evaluate the quasi-shear stress at the cavity endwall. The hot-film gauges are spread over two inserts. Figure 2.31 shows different view of the endwall inserts equipped with hot-films mounted in the cascade. All the sensors have the same dimensions (width of 0.1016 mm, thickness of 0.0002 mm and length of 1.4478 mm).

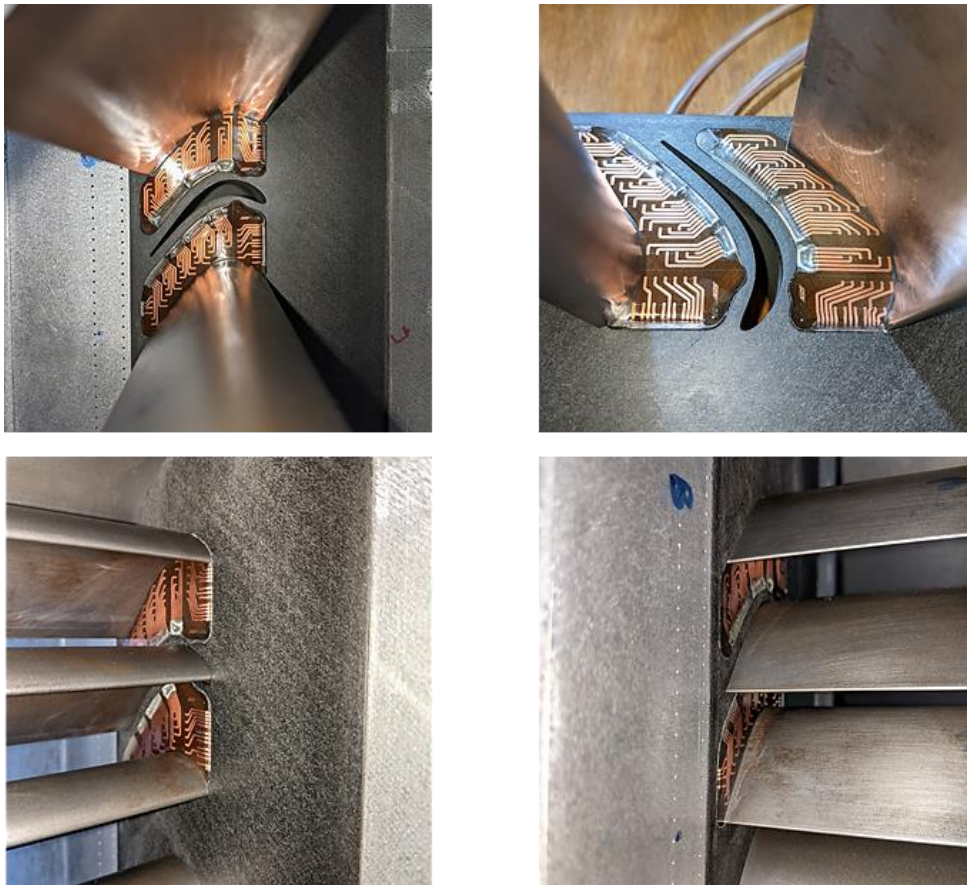

Figure 2.31: HF Instrumented endwall inserts.

2.2.6 Sensors and signal conditioning

The characteristics of the fixed instrumentation used during the experimental campaign reported here are presented below in Table 2.3.

Table 2.3: Fixed instrumentation.

Type	Channels	Range	Accuracy [% FS]	Accuracy [Pa]
WIKA P-30 Absolute pressure sensor	1	25 000 Pa	0.1% FS	25 Pa
MPS4264/64NPx- 2.5 PSID	64	17 237 Pa	0.08% FS	14 Pa
MPS4264/64NPx- 1 PSID	64	6895 Pa	0.06% FS	4 Pa
Validyne Sensor (350 Pa)	1	350 Pa	0.5% FS	2 Pa

2.2.6.1 *Absolute pressure sensor*

The total pressure at the inlet of the test section $P_{0,ref}$ is monitored during the experiments with the absolute pressure sensor WIKA P-30. A photo of the sensor is presented in Figure 2.32.

Figure 2.32: WIKA P-30

2.2.6.2 Pressure scanners

Two Scanivalve MPS4264 miniaturized piezoresistive pressure sensors with a range of 1 psi and 2.5 psi are used to record the pressure inside the test section. The arrangement is depicted in Figure 2.33. Each Scanivalve has 64 channels, for a total of 128 channels.

Figure 2.33: MPS4264/64NPx- 2.5 PSI and 1PSI.

In the presented experimental campaign, two the scanners are used to acquire pressure information concerning:

- Reference total pressure $P_{0,ref}$.
- Static pressure from the wall taps relative to the various measurement planes.
- Cascade base pressure.
- Pneumatic probes.

The pneumatic taps located on the pneumatic probe heads, blade as well as endwall surfaces are directly connected to the Scanivalve pressure sensors by means of pneumatic pipes. A special interface is used to allow the routing of the pipes from the inside of the wind tunnel to the lab and then to the scanners' connections. A figure showing the interface and the pneumatic pipes is depicted in Figure 2.34. A 3D printed part is used to support the pneumatic pipes with the aim of avoiding leakages.

Figure 2.34: Pneumatic connector and 3D printed support.

The MPS4264 integrates all the electronics for the analog-to-digital conversion of the signal. Therefore, the scanners are connected to the measurement PC directly through an Ethernet connection.

2.2.6.3 Validyne differential pressure sensor

One Valydine DP15-42 sensor, depicted in Figure 2.35, is used to monitor and acquire the total pressure at the inlet of the cascade. In particular, the sensor is connected to the redundant total pressure probe and gives the value of $P_{0,ref,bis}$ referenced to the laboratory ambient pressure. The signal is demodulated and amplified before being acquired with the fast response acquisition system.

Figure 2.35: Valydine DP15-42.

2.2.6.4 *Fast-response pressure sensors*

Two types of fast-response pressure sensors are used in the current experimental campaign. The details of the sensors are reported in Table 2.4. Throughout the experimental campaign, the Kulite sensor signals have been low-pass filtered at 250 kHz (analogue anti-aliasing filter) and subsequently digitally low-pass-filtered at 30 kHz.

Table 2.4: Kulites sensors characteristics.

Type	Range	Accuracy [% FS]	Accuracy [Pa]
Kulite: XCQ-062 (abs. 5PSI)	34 474 Pa	0.1%	35 Pa
Kulite: LQ-062 (abs. 5PSI)	34 474 Pa	0.1%	35 Pa

2.2.6.5 *Constant-temperature anemometry*

The anemometer used in the framework of the present experimental campaign is the Dantec Dynamics Streamline Pro, shown in Figure 2.36. It consists in six integrated and independent modules. Each of the modules consist in a CTA control circuit, composed of bridge and feedback amplifier followed by a signal conditioner. A single module can operate independently from the others, which means that potentially 6 probes or sensors can be used simultaneously. The whole system is operated through a dedicated software provided by Dantec Dynamics called Streamware Pro running on a dedicated PC. The anemometer is used for both hot-wire and hot-films measurements.

Figure 2.36: Dantec Dynamic Streamline Pro Constant Temperature Anemometer.

The operating temperature of the both wires and hot-film sensors, is chosen accordingly to the to the flow temperature expected during the measurements and is kept fixed during the measurements.

Each of all the available 6 anemometer channels is tuned for each measuring sensor. For the surface hot-film gauges, an over-heat ratio of 0.50 was selected to achieve a sensor temperature of +60 K with respect to a prescribed reference temperature, close to the ambient temperature. For the hot-wire probes, an over-heat ratio of 0.76 was selected to achieve a wire temperature of about 500 K with respect to a typical flow temperature of 300 K.

To adjust the response of the sensor-anemometer ensemble, a square-wave test is performed before the productive measurements. The square wave test also provides an estimation of the frequency response of the system. All sensors underwent a square wave test to assess the sensor operating bandwidth.
Surface hot-films placed on the blade featured a bandwidth comprised between 50 and 100 kHz. Hot-film sensors operated on the cascade endwall showed a bandwidth comprised between 30 and 65 kHz.
The bandwidth of the probes P-HW-01 and P-HW-02 (equipped with 9 μm tungsten wires) was found to be in the order of 9-10 kHz.

All the measured signals go through an analogue anti-aliasing low-pass filter prior to digitalization. The hot-wire signals were filtered at 30 kHz, whereas the surface hot-film signals were filtered at 100 kHz.

2.2.7 Data acquisition systems and acquisition settings

Beside the scanivalve pressure measurement systems, analogue signals are digitalized and acquired using two acquisition cards: one NI6250-DAQ and one high-speed data acquisition card NI6253-USB.

The NI6250-DAQ is constituted of a chassis containing 3 NI6250 PCI cards with each 16 inputs at 16-bits digital resolution. Each card has a total sampling frequency of 1 MHz that is shared equally between the active channels being used. During normal operation, the NI6250-DAQ is used to sample the signals coming from the reference pressure Valydine and the reference thermocouple.

The high–speed data acquisition card NI6253-USB, has 8 channels at 16-bits digital resolution and a max sampling frequency of 1.20 MHz per channel. This board is used to acquire the signals of: the fast-response pressure sensors (blade, endwalls and probes), hot-wire probes, hot-film gauges (blade and endwalls), and wake generator photodiode.

All low-bandwidth pressure measurements are sampled over 2 seconds at 300 Hz. Acquisitions of pressure measurements from pneumatic probes or instrumented blades are initiated 6 seconds after the instrumentation has reached the next measuring point to account for the pressure line time lag when traversing in flows with large gradients at relatively low absolute pressures (P ~ 4,000 -10,000 Pa).

The fast-response surface hot-film and piezo-resistive pressure sensors were acquired over 3 seconds at 1.2 MHz.
The measurement signals from the hot-wire probe P-HW-01, traversed in Plane 02 to sample the boundary layer (over the two central pitches from the blade midspan up to 0.3 mm far from the endwall), were acquired at 70 kHz over 5 seconds.
The measurement signals from the hot-wire probe P-HW-02 probe, traversed in Plane 02 at the cascade mid-span (across the two central pitches with a resolution of 1 mm) were acquired at a frequency of 1.2 MHz for 3 seconds.

3 Experimental flow conditions

This chapter details the determination of the real experimental flow conditions achieved in the wind tunnel during the measurements. The aim of the following sections is to present the definitions of the parameters used to define the test conditions and the methods used to compute and set the desired flow conditions during the experiments.

3.1 Definition of flow conditions

The flow conditions in the test section are measured continuously by monitoring the total temperature and pressure upstream of the cascade and the static pressure at the cascade inlet and outlet. During the experimental campaign detailed in this report, and for the sake of the computation of the computation on the operating conditions, Plane 01 is considered as inlet plane (in), while Plane 06 is used as outlet plane (out). the procedure applied to compute the operating conditions is described hereafter.

The experimental campaign of the SPLEEN C1 cascade aims at accurately reproducing engine representative conditions as observed in modern high-speed LPTs. Since the measurements concern the cascade aerodynamics, the important quantities to reproduce are the free-stream exit Mach and Reynolds numbers, inlet free-stream turbulence intensity and scales, periodic incoming wakes (Strouhal number, flow coefficient), the geometry of the cavities and the characteristics of the leakage flow. The main relevant flow conditions in the cascade are the isentropic downstream Mach and Reynolds numbers, $M_{out,is}$ and $Re_{out,is}$ (based on the airfoil chord length) respectively, and the background free-stream turbulence intensity Tu and integral length scale.

3.1.1 Determination of the cascade inlet total pressure

The loss coefficient of the passive, stationary turbulence grid is Y_{TG}, while the loss coefficient of the periodic WG is Y_{bars}. Once these loss terms are known, the inlet total pressure to the blade cascade $P_{0,in}$ can be evaluated from the reference total pressure $P_{0,ref}$ through the following equations, depending on whether the turbulence grid or the periodic WG or both are used.

No grid – No bars	$P_{0,in} = P_{0,ref}$
Grid – No bars	$P_{0,in} = (1 - Y_{TG}) \cdot P_{0,ref}$
No grid – Bars	$P_{0,in} = (1 - Y_{bars}) \cdot P_{0,ref}$
Grid – Bars	$P_{0,in} = (1 - Y_{tot}) \cdot P_{0,ref}$

Where Y_{tot} represents the combination of the pressure losses originating from the turbulence grid and the wake generator's bars. Please note that both the turbulence grid and WG losses are experimentally evaluated during the commissioning phase of the test campaign. The evaluation of Y_{tot} is achieved during the experimental phase 2 where the WG is installed in front of the turbine cascade.

Being the pressure drop coefficient across the turbulence grid, Y_{TG} can be defined as:

$$Y_{TG} = \frac{P_{0,ref} - P_{0,in}}{P_{0,ref}}$$

The Y_{TG} computed by studying the turbulence grid individually. Measurements of the total pressure upstream of the cascade in the pitchwise direction allow to isolate the losses due the turbulence grid and friction losses.

This allows to compute the total pressure upstream of the cascade:

$$P_{0,in} = P_{0,ref}\ (1 - Y_{TG})$$

3.1.2 Cascade Mach and Reynolds numbers

The evaluation of the inlet total pressure, $P_{0,int}$ allows the computation of the other flow conditions. For instance, the $M_{in,is}$ is computed from the measured $P_{in,s}$ (static pressure in Plane 01) and the inlet total pressure, $P_{0,in}$, by the following equation:

$$M_{in,is} = \sqrt{\frac{2}{\gamma - 1}\left[\left(\frac{P_{in,s}}{P_{0,in}}\right)^{-\frac{\gamma-1}{\gamma}} - 1\right]}$$

The computation of the cascade outlet isentropic Mach number, $M_{out,is}$, is performed with the following equation:

$$M_{out,is} = \sqrt{\frac{2}{\gamma - 1}\left[\left(\frac{P_{out,s}}{P_{0,in}}\right)^{-\frac{\gamma-1}{\gamma}} - 1\right]}$$

The two quantities required to compute $M_{out,is}$ are the cascade outlet static pressure, $P_{out,s}$, and total pressure upstream of the cascade, $P_{0,in}$. The former is determined by means of the pressure taps situated downstream of the blades TE in plane 06. The latter is computed from the total pressure drop coefficient from the measurement of the reference total pressure upstream of the turbulence grid.

The computation of the Reynolds number based on the outlet quantities is performed using the equation:

$$Re_{out,is} = \frac{\rho_{out,is}\, c\, V_{out,is}}{\mu_{out,is}}$$

Since the chord, c, is fixed throughout the experimental campaign, the parameters affecting the Reynolds number are only the cascade outlet isentropic density, $\rho_{out,is}$, velocity, $V_{out,is}$, and dynamic viscosity, $\mu_{out,is}$. The former can be obtained if the cascade outlet static temperature, $T_{out,s}$, and static pressure, $P_{out,s}$, are known. The equation to be used in the determination of $\rho_{out,is}$:

$$\rho_{out,is} = \frac{P_{out,s}}{R\, T_{out,s}}$$

The cascade outlet static temperature is computed from the previously determined $M_{out,is}$ and $T_{0,in}$. Knowing these two quantities, the following isentropic equation can be used to determine $T_{out,s}$:

$$T_{out,s} = T_{0,in}\left(1 + \frac{\gamma - 1}{2} M_{out,is}^2\right)^{-1}$$

$V_{out,is}$ is also computed from $M_{out,is}$ and $T_{out,s}$ as follows:

$$V_{out,is} = M_{out,is}\sqrt{\gamma R T_{out,s}}$$

Where $\gamma = 1.40$ and $R = 287.06$.

Lastly, $\mu_{out,is}$ can be solely computed from the outlet static temperature using the Sutherland's law:

$$\mu_{out,is} = \frac{1.458 \times 10^{-6}\, T_{out,s}^{\frac{3}{2}}}{T_{out,s} + 110.4}$$

Using the previous quantities, $Re_{out,is}$ can be computed as:

$$Re_{out,is} = \frac{\rho_{out,is}\, V_{out,is}\, C}{\mu_{out,is}}$$

3.1.3 Strouhal number and flow coefficient of unsteady inlet wakes

The measurements of the wake generator rotational speed (RPM) together with the number of bars and the outlet flow velocity $V_{out,is}$ is used to determine the Strouhal number and the flow coefficient associated with the incoming wakes. The Strouhal number is defined according to:

$$St = \frac{RPM}{60}\, N_{bars}\, \frac{c}{V_{out,is}}$$

Where the RPM is the wake generator speed expressed in round per minute and *c* is the airfoil chord. The flow coefficient is computed as the ratio of the inlet axial velocity to the peripheral velocity of the bars:

$$\Phi = \frac{V_{in,x}}{U}$$

In this equation, the inlet axial velocity can be computed from the inlet Mach number, flow total temperature and inlet flow yaw angle, according to:

$$V_{in,x} = M_{in}\sqrt{\gamma R T_{in,s}}\cos\beta_{in}$$

The peripheral bar velocity is computed from the rotational speed of the WG and the distance from the center of rotation to the region of interest.

$$U = \frac{2\pi \times RPM}{60} r$$

3.2 Turbulence grid loss coefficient

The need for a method to evaluate the turbulence grid losses originates from the necessity to know the cascade inlet total pressure downstream of the turbulence grid (Plane 01) when no probe is mounted at this specific location. In particular, the total pressure is needed to compute the cascade operating conditions, both during the experiments and in the post-processing phase, and a dedicated probe cannot be installed in Plane 01 during each test as it would create problems related to probe intrusiveness. To overcome this, a correlation for the computation of the turbulence grid losses Y_{TG} is built. The procedure applied is as follows:

- Total pressure probe (P-BL-01) is mounted in the test section. The probe stem inserted in the slot in Plane 02. The probe head is traversed in Plane 01.
- The pressure value measured by the probe is used during the test to compute the downstream $M_{6,is}$ and $Re_{6,is}$ and set the flow conditions.
- P-BL-01 probe is traversed in the pitch direction (pitches [-1; +1]) at midspan to sample the pitch-wise distribution of P_{01}.
- The procedure is repeated for all on- and off-design flow conditions ($M_{6,is} = 0.70 \div 0.9$; $Re_{6,is} = 65k \div 120k$).

Two sketches showing the P-BL-01 mounted in the test section, with the probe head located in Plane 01, as well as the probe traversing direction are presented in Figure 3.1.

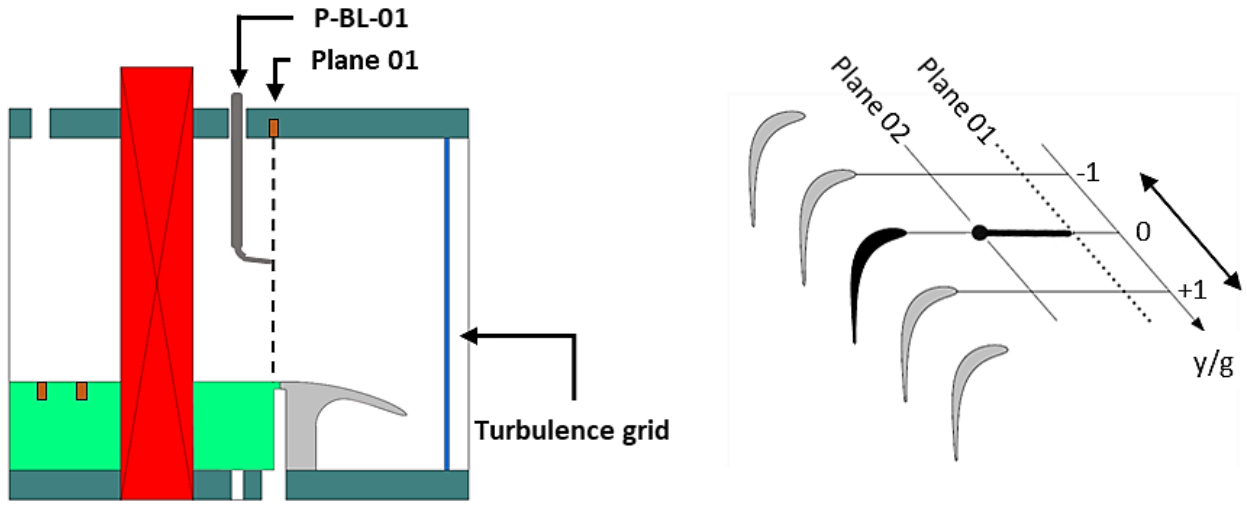

Figure 3.1: Measurement setup for characterization of TG losses.

The total pressure probe was traversed for all the combinations of flow conditions presented in Table 3.1:

Table 3.1: Flow conditions for Y_{TG} investigation.

$Re_{6,is}$	$M_{6,is}$
65000	0.90
65000	0.80
65000	0.70
70000	0.95
70000	0.90
70000	0.80
70000	0.70
100000	0.95
100000	0.90
100000	0.80
100000	0.70
120000	0.95
120000	0.90
120000	0.80
120000	0.70

The total pressure loss coefficient Y_{TG} is computed according to the equation below:

$$Y_{TG} = \frac{P_{0,ref} - P_{0,in}}{P_{0,ref}}$$

The distribution of total pressure loss coefficient is shown in Figure 3.2 for all tested conditions. The left plot in the figure reports the absolute value of Y_{TG}. The loss coefficient follows a clear trend as it increases for increasing outlet Mach numbers (corresponding to increasing inlet Mach numbers). The Reynold effect on the turbulence grid losses is also evident from the figure, higher $Re_{6,is}$ for a given $M_{6,is}$ determines higher Y_{TG}.

Furthermore, the distribution of Y_{TG} shows a pitch-wise distortion. To allow comparison of the distortion shape for all the tested conditions, the values presented in the right plot of Figure 3.2 are normalized by the mean pitch-wise value for each condition. The shape of the distortion is nearly identical for all cases. Considering that Y_{TG} is used to compute the cascade inlet flow conditions during the post-processing phase, the effect of the pitch-wise variation determined by the distortion on the computed flow condition must be estimated. The evaluation is done for the nominal flow conditions ($Re_{6,is}$=70k; $M_{6,is}$=0.9). The Y_{TG} maximum (located in y/g = 1.06 [-]) and minimum (located in y/g = 0.18 [-]) values are used to compute the variation of P_{01} that would originate from using those values instead of the mean Y_{TG} to obtain P_{01} in the processing phase. The following equation are applied:

$$P_{01} = (1 - Y_{TG}) \cdot P_{0,ref}$$
$$P_{01,maxloss} = \left(1 - Y_{TG,max}\right) \cdot P_{0,ref}$$
$$P_{01,minloss} = \left(1 - Y_{TG,min}\right) \cdot P_{0,ref}$$
$$\Delta P_{01} = P_{01,minloss} - P_{01,maxloss}$$

The typical value of $P_{0,ref}$ for the nominal flow conditions is used. The inlet distortion translates in a spatial variation of inlet total pressure $\Delta P_{01} = 23\ Pa$, that remains within the pressure measurement uncertainty.

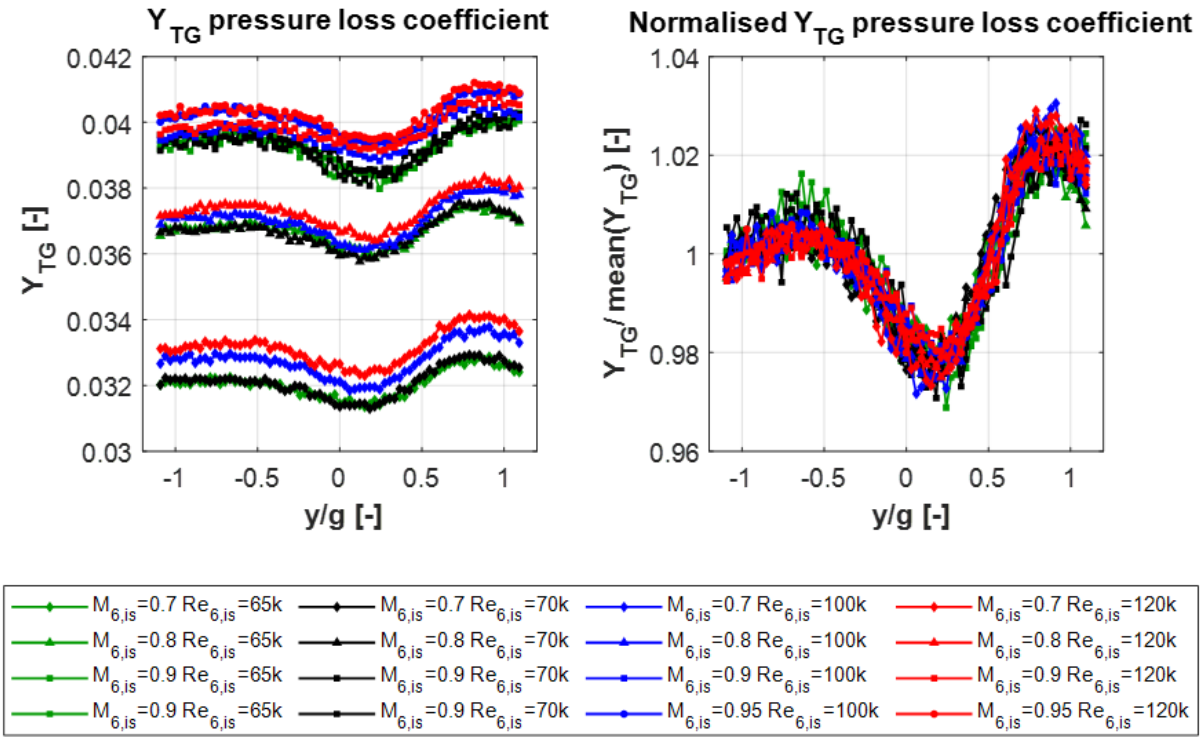

Figure 3.2: Pitchwise distribution of Y_{TG}. Absolute (left) and normalised over the pitch-wise mean (right).

Figure 3.3 shows the pitchwise averaged Y_{TG} for all tested conditions. The loss coefficient follows an increasing trend with the outlet and inlet Mach numbers. The Reynolds effect on the turbulence grid losses is also evident, as higher $Re_{6,is}$ for a given $M_{6,is}$ yields higher Y_{TG}.

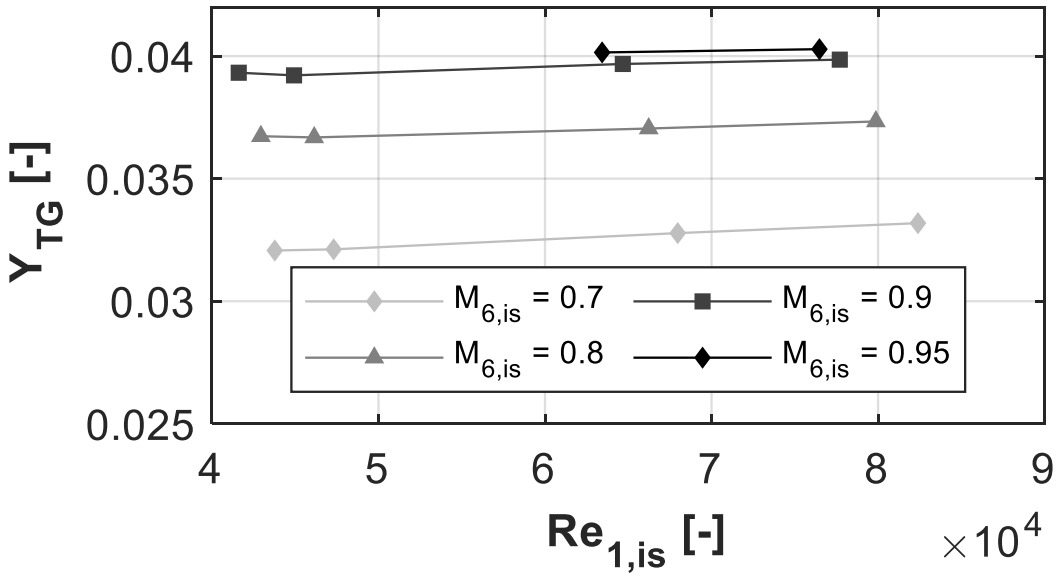

Figure 3.3: mean value of Y_{TG} for all tested conditions.

The repeatability of the turbulence grid loss coefficient is presented in Figure 3.4. The results obtained for two tests are compared in the plot. The difference between the two curves is propagated on the cascade inlet total pressure calculation using the equations presented directly above. The calculation is done for each pitch-wise measurement location and only the maximum difference is reported here. The maximum variation between the two curves is ΔY_{TG} = 0.0684 %. This variation translates to a maximum variation of inlet total pressure ΔP_{01}

= 6.56 Pa. Therefore, the comparison shows that the shape of the inlet pressure distortion is repeatable and that the error on the computation of the inlet total pressure remains well within the measurement uncertainty.

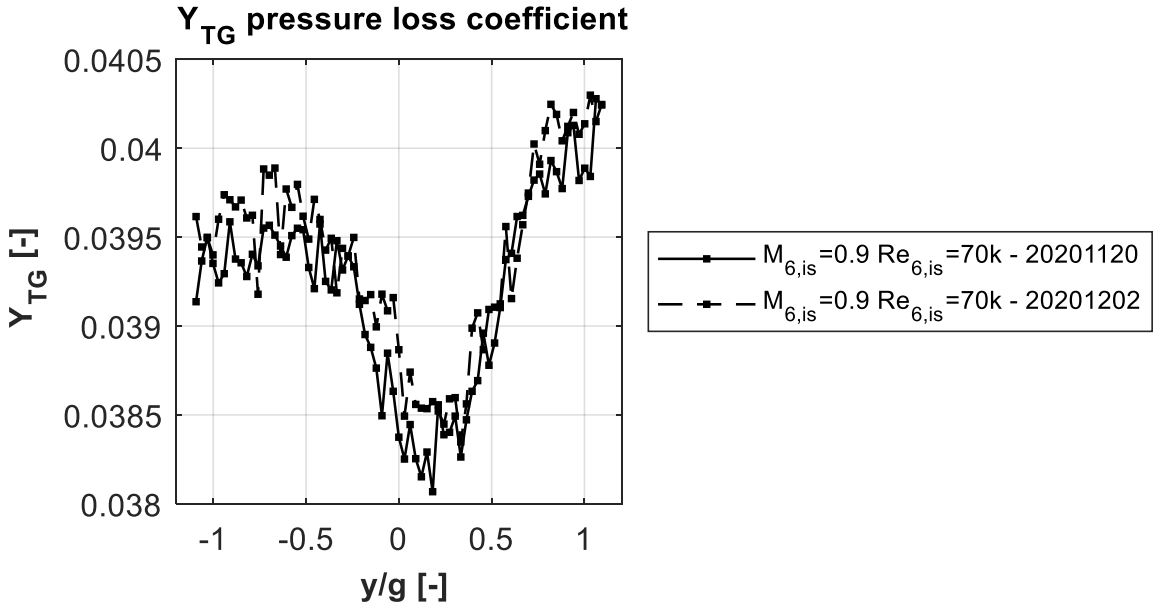

Figure 3.4: Repeatability of pitch-wise distribution of Y_{TG}.

The experimental data presented in Figure 3.2 was used to create two correlations to link the experimentally computed values of Y_{TG} with the flow conditions at the cascade inlet and outlet computed with the quantities measured during the experiments. In other words, the inlet correlation allows the computation of Y_{TG} given the values of $Re_{1,is}$ and $M_{1,is}$ obtained from the fixed cascade instrumentation located in Plane 01. Similarly, the outlet correlation is based on $Re_{6,is}$ and $M_{6,is}$ values measured in Plane 06.

The inlet total pressure estimated with the correlations was verified to agree very well with the one measured by the total pressure probe. The maximum difference between pressure computed by correlations and that measured by a traversing probe was $\Delta P_{01,\ probe-corr,\ max} = 9\ Pa$.
Throughout the whole traverse, the correlation to predict the inlet and outlet Mach numbers have shown good level of agreement with the probe measured data. The maximum variation between correlation-based Mach numbers and probe measurements has been verified to be lower than 0.001.

The correlation for the prediction of the outlet Reynolds number agrees with the probe-measured data throughout the whole traverse. The maximum discrepancy remains within the uncertainty of the measurement $\Delta Re_{6,is\ \ probe-corr,\ max} \sim 100$.

The validation of the correlations leads to the conclusion that the in-situ calibrated correlations can be used to accurately compute the value of the turbulence generator pressure loss coefficient Y_{TG} for the desired outlet flow conditions.

3.3 Total pressure loss coefficient

Once the wake generator is introduced downstream the turbulence generator, it is necessary to define the total losses of these two components to define the operating conditions of the cascade. Therefore, a correlation for the computation of the total losses Y_{tot} is built, including the wake generator losses and the turbulence grid losses. The procedure applied is as follows:

- Cobra-shaped five-hole probe (P-C5HP-01) is traversed in Plane 02 in the pitch direction (pitches [-1; +1]) at midspan.
- The pressure value measured by the probe is used during the test to compute the downstream $M_{6,is}$ and $Re_{6,is}$ and set the flow conditions.
- The procedure is repeated for all the on- and off-design flow conditions ($M_{6,is} = 0.70 \div 0.95$; $Re_{6,is} = 65k \div 120k$).

Two sketches showing the P-C5HP-01 mounted in the test section, as well as the probe traversing direction are presented in Figure 3.5.

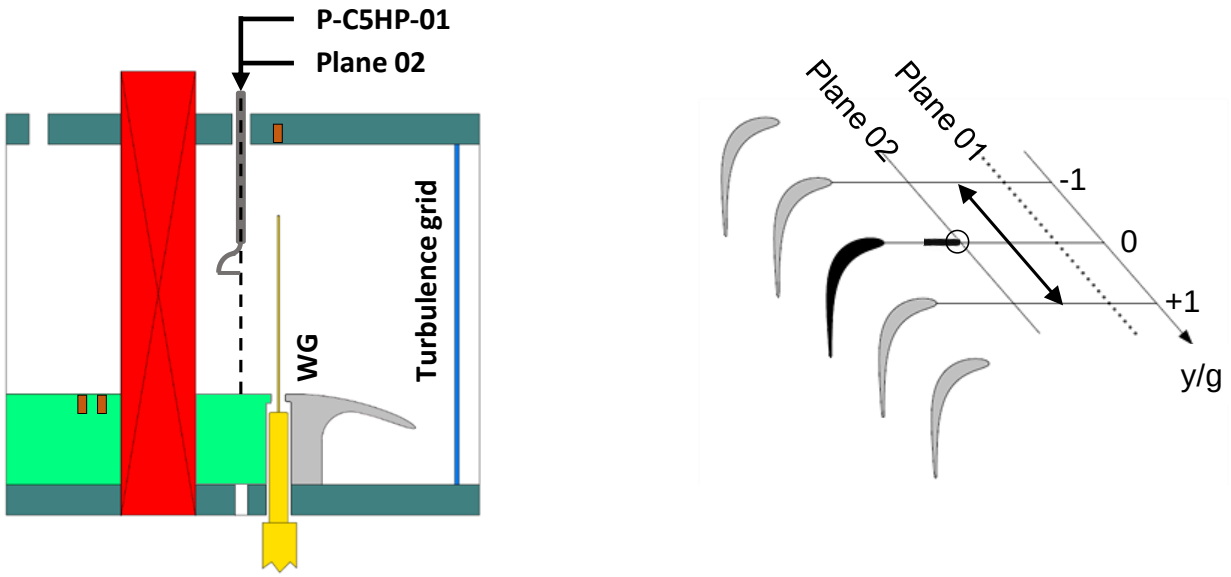

Figure 3.5: Measurement setup for the characterization of the total losses (WG + TG).

The total pressure probe was traversed for all the combinations of tested flow conditions, summarized in Table 3.2:

Table 3.2: Flow conditions for Y_{tot} investigation.

$Re_{6,is}$	$M_{6,is}$
65000	0.60
65000	0.90
70000	0.60
70000	0.70
70000	0.80
70000	0.90
70000	0.95
100000	0.95
100000	0.90
120000	0.80
120000	0.70

The total pressure loss coefficient Y_{tot} is computed according to:

$$Y_{tot} = \frac{P_{0,ref} - P_{02}}{P_{0,ref}}$$

The distribution of total pressure loss coefficient is shown in Figure 3.6 for all tested conditions. The absolute value of Y_{tot} is reported in the left-hand side plot of the figure. The losses follow a clear trend, increasing for increasing outlet Mach numbers (and increasing inlet Mach numbers).

A pitch-wise distortion is present, likewise to the Y_{TG} distribution shown in Figure 3.2. To evaluate the independence of the pitchwise shape to the flow conditions, the right-hand side plot in Figure 3.6 presents the pitchwise distributions of Y_{tot} normalized by the mean value for each condition. The shape of the distortion is identical for all cases. An average value of Y_{tot} is used to compute the cascade inlet flow conditions during the post-processing phase, therefore the effect of the pitch-wise distortion on the computed flow condition must be estimated. For the nominal flow conditions ($Re_{6,is}$=70k; $M_{6,is}$=0.9), the variation of P_{02} corresponding to the variation of the Y_{tot} between the maximum (located in $y/g = +1.03$) and minimum (located in $y/g = -1.36$) values is computed according to the following equations:

$$P_{02} = (1 - Y_{tot}) \cdot P_{0,ref}$$
$$P_{02,maxloss} = \left(1 - Y_{tot,max}\right) \cdot P_{0,ref}$$
$$P_{02,minloss} = \left(1 - Y_{tot,min}\right) \cdot P_{0,ref}$$
$$\Delta P_{02} = P_{02,max} - P_{02,min}$$

When the value of $P_{0,ref}$ for the nominal flow conditions is used, the inlet distortion translates into a total pressure variation of $\Delta P_{02} = 23\ Pa$, which is within the pressure measurement uncertainty.

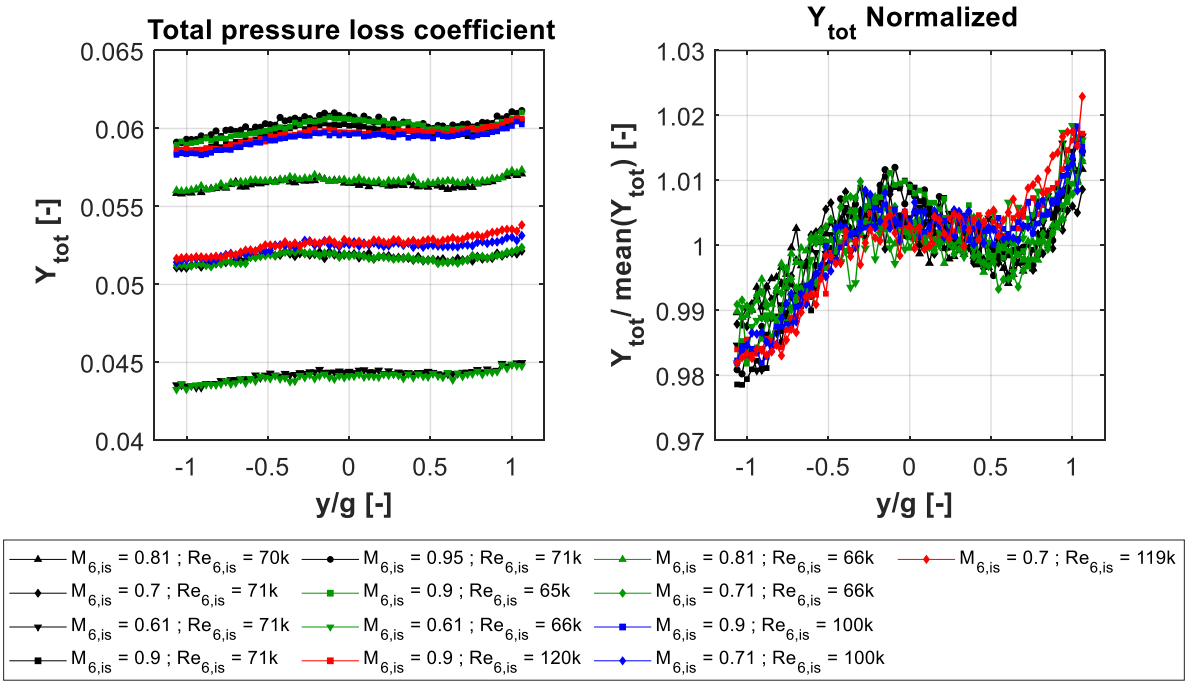

Figure 3.6: Pitchwise distribution of Y_{tot}. Absolute (left) and normalized over the pitch-wise mean (right). Testing phase with wake generator.

The values of Y_{tot} obtained from the correlations for each flow conditions are used in analogous way than for the cases with the turbulence grid only.

The maximum difference between total pressure computed by correlations and those measured by probes lies well within the uncertainty band of the measurement itself, $\Delta P_{01,\ probe-corr,\ max} = 9\ Pa$.

The maximum difference in flow Mach number predictions and measurements is also within the uncertainty of the measurement $\Delta M_{1,is\ \ probe-corr,\ \ max} < 0.007$.

The maximum difference in flow Reynolds number predictions and measurements is within the uncertainty of the measurement $\Delta Re_{1,is\ \ probe-corr,\ \ max} < 700$.

The validation of the correlations confirmed the conclusion found in the tests with the turbulence generator only, that the correlation to predict the combined pressure loss of turbulence grid and wake generator (Y_{tot}) can be used to precisely estimate the inlet total pressure in the absence of a fixed total pressure probe in test section upstream planes 01 and 02.

3.4 Setting the flow conditions

During the operation of the wind tunnel, the operator controlling the facility can act on two separate parameters to regulate the flow conditions: the rotational velocity of the compressor and the opening of the tunnel pressure regulation valve. The information needed for the regulation is obtained from the data sampled by the acquisition system and is displayed in real time on the control PC. Details of the fixed instrumentation data used to compute the live flow conditions are presented in Table 3.3.

Table 3.3: Acquisition of fixed instrumentation data.

Quantity	ACQ system
$P_{0,ref}$	WIKA, Scanivalve scanners 2.5 PSI channel 1
$T_{0,ref}$	NI6250 channel 2
$P_{1,s}$	Scanivalve scanners 1 PSI channels 2-32
$P_{6,s}$	Scanivalve scanners 2.5 PSI channels 3-62
$P_{base,s}$	Scanivalve scanners 2.5 PSI channels 64

Given that the duration of a single probe traverse can last for more than 7 hours, the rig flow conditions can vary. The variation of the ambient conditions does not strongly influence the conditions inside the wind tunnel. The main effect of continuous operation is the heat transfer between the compressor and the flow. Thus, the air in the facility experiences a temperature drift during the experiments, which needs to be accounted for. Therefore, the independent regulation of the compressor RPM and the accurate control of the pressure are required to obtain constant outlet isentropic Mach and Reynolds numbers.

In addition to the natural variation of the flow conditions during long operations, a supplementary complication arises from the insertion of probes in the test section. Two problems can be associated with the probe interference regarding the cascade operating conditions: the setting of the target flow conditions for the measurements and the monitoring of their stability. In fact, independently of the plane of measurement, the presence of a probe in the test section has an influence on the endwall pressure taps used to set and monitor the flow field. Furthermore, as the probe head approaches the endwall taps, the readings of those taps become unusable.

To clarify the effect of the probe traverse on the operation of setting accurate flow conditions, a typical signature of inlet and outlet Mach and Reynold numbers computed during a typical P-L5HP-01 2D traverse in Plane 06 at the nominal flow conditions are reported in Figure 3.7 and Figure 3.8. The plots present the values of Mach and Reynolds calculated by averaging the pressure obtained with an increasing number of endwall taps. The x-axis of the plots represents the number of acquisitions, i.e. the traverse duration.

Figure 3.7 shows that the interference effect of the probe traversing in the downstream plane on the computed inlet values can be reduced by averaging the complete set of available taps.

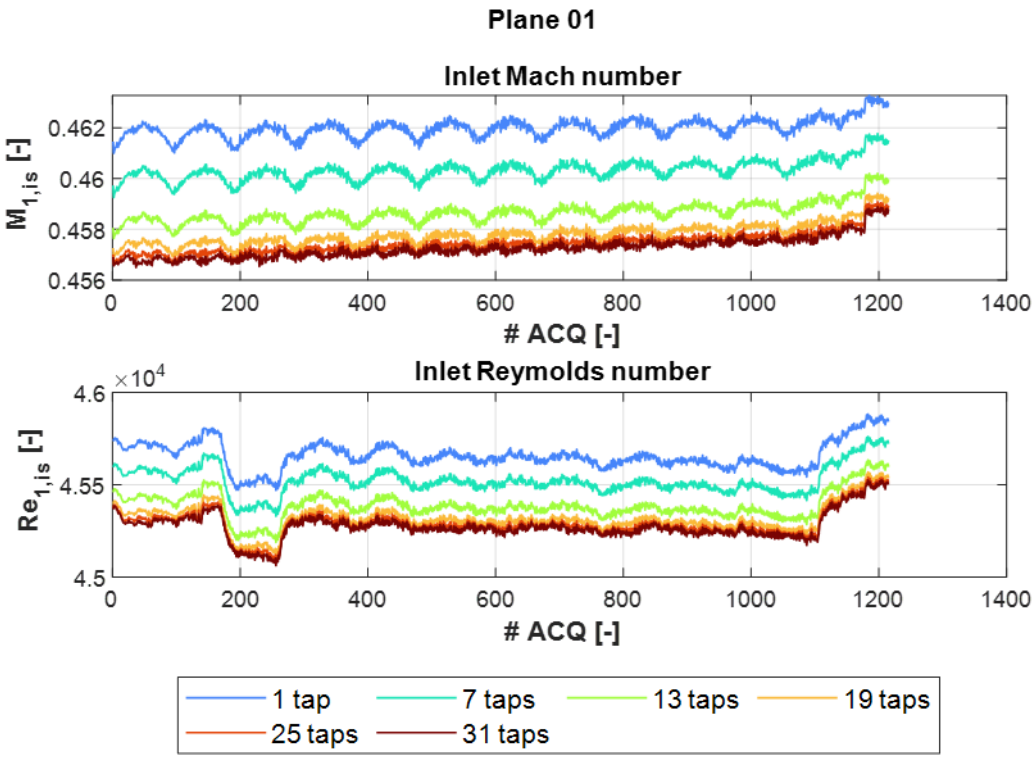

Figure 3.7: Evolution of inlet Mach and Reynolds during a 5HP traverse in Plane 06 obtained by averaging the readings of different number of endwall taps.

Regarding the outlet flow conditions reported in Figure 3.8, since the head of the L-5HP probe is traversed in the same plane of the endwall pressure taps, the influence on the calculated Reynolds and Mach numbers is stronger. It must be underlined that the variations visible in the plot are not representative of variations of the conditions in the complete test section, but only of the computed values as a direct local effect of the probe moving in the measurement plane. Reducing the number of averaged taps is in this case beneficial, because it allows to eliminate from the computation the taps that are most influenced by the probe effect. Taking into consideration only taps between 7 and 13 permits to track the flow conditions with reduced variability and acceptable stability.

To demonstrate that the local effect of the probe head does not influence the whole cascade flow, $M_{base,is}$ and $Re_{base,is}$ obtained from the base pressure taps are also included in the plots in Figure 3.8. The stability of the set conditions is proven by the small impact that the probe traversing has on the reading of the base pressure tap. More details about the use of the base pressure taps for the quantification of flow stability is reported in section 3.5.

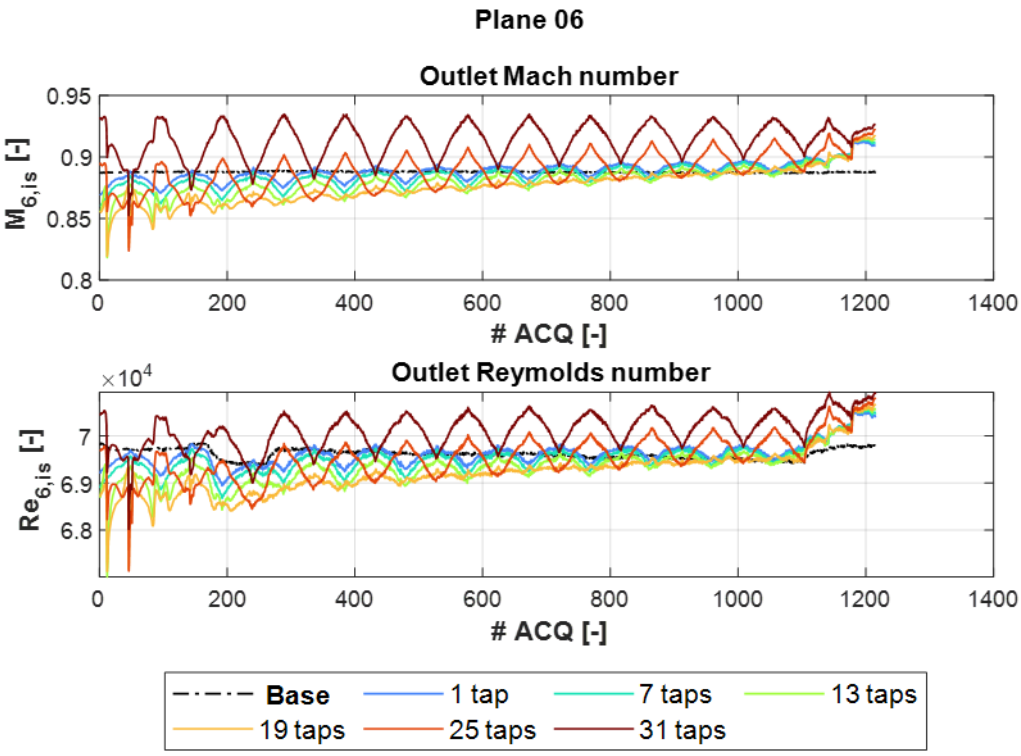

Figure 3.8: Evolution of outlet Mach and Reynolds during a 5HP traverse in Plane 06 obtained by averaging the readings of different number of endwall taps.

The data presented above is used to inform the methodology used to set and maintain the correct flow conditions. The resulting configuration employed during the flow conditions setting procedure is presented in the sketches in Figure 3.9. The diagram on the left-hand side of the figure is representative of a test with probe inserted in Plane 02. The probe is positioned at the pitch position $y/g = +1$ and only the first 7 pressure taps on the negative-value pitch are used to compute the inlet flow conditions, while data from all the Plane 06 taps is used to compute the outlet Reynold and Mach numbers. The number of used taps originates from a study like the one presented in Figure 3.7 and Figure 3.8.

Similarly, for the downstream probe measurements, during the setting of the flow conditions, the probe is positioned in $y/g = +2$ and 50% span. Only the first 10 taps are used to compute $M_{6,is}$ and $Re_{6,is}$. The procedure introduced here permits to reduce as much as possible the intrusiveness of the probe during the setting of the conditions in the test section. A summary of the procedure is presented in Table 3.4.

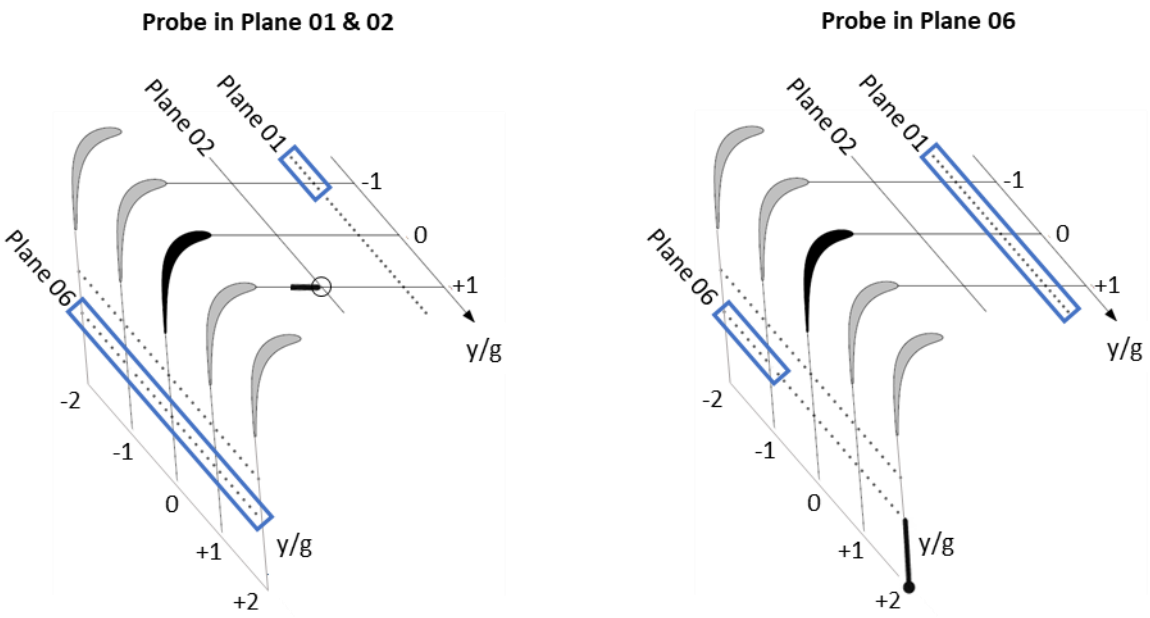

Figure 3.9: Sketches representing the location of the probe at the inlet planes 01 and 02 (left) and at the outlet plane (right) during the flow conditions setting procedure. The figure shows also the taps used to set the outlet and inlet Mach and Reynolds numbers in the two cases.

Table 3.4: Probe location and averaged taps for flow conditions setting.

Plane	Probe pitch [y/g]	Probe span	Taps
Plane 01	+1	50%	1-7
Plane 02	+1	50%	1-7
Plane 06	+2	50%	1-10

It is worth mentioning that in case no probe is inserted in the test section no interference problem is reported during operations. Therefore, all the pressure taps are used to assess the flow conditions.

3.5 Monitoring the test operating conditions by the cascade base pressure

As already mentioned in the description of Figure 3.8, the pressure tap located at the base of the cascade ($P_{base,s}$) represents an important tool to set and monitor the flow conditions in the test section during operation. The reading from the tap can, in fact, be used to evaluate the values of $M_{base,is}$ and $Re_{base,is}$ that are monitored during the data acquisition procedure. Since the tap is located far from the probe moving in the test section, the computed parameters are representative only of the overall cascade flow conditions and can be used independently on the presence of a probe in the downstream plane. The black dashed line in Figure 3.8 shows that the base pressure tap is not influenced by the probe and that the flow conditions during the acquisition are stable.

In order to further expand the use of the base pressure tap as a tool to evaluate and monitor the stability of the flow conditions, data acquired during multiple days of testing at on-and off-design without probe, i.e. with clean flow in the test section, can be used to build a correlation between the conditions at the cascade base and the conditions in the test section. In other words, $M_{base,is}$ and $Re_{base,is}$ can be correlated to $M_{6,is}$ and $Re_{6,is}$. Therefore, this correlation enables the evaluation of the operating conditions downstream of the cascade even when performing traverses with the probe.

The data used to build the dataset are representative of the on- and off-design operating conditions reported in Table 3.5.

Table 3.5: Flow conditions for base correlation study.

$Re_{6,is}$	$M_{6,is}$
65000	0.90
65000	0.70
70000	0.95
70000	0.90
70000	0.70
120000	0.90
120000	0.70

Two polynomial surfaces of second order in $M_{base,is}$ and of the first order in $Re_{base,is}$ are used to fit the values of $M_{6,is}$ and $Re_{6,is}$. The equations are of the kind presented below:

$$M_{6,is}\left(M_{base,is}, Re_{base,is}\right) = C_1 + C_2 \times M_{base,is} + C_3 \times Re_{base,is} + C_4 \times M_{base,is}^2 + C_5 \times M_{base,is} \times Re_{base,is}$$

$$R_{6,is}\left(M_{base,is}, Re_{base,is}\right) = C_1 + C_2 \times M_{base,is} + C_3 \times Re_{base,is} + C_4 \times M_{base,is}^2 + C_5 \times M_{base,is} \times Re_{base,is}$$

The resulting surfaces are reported in Figure 3.10, while the values of the coefficients and of the R^2 for the two correlations are reported in Table 3.6.

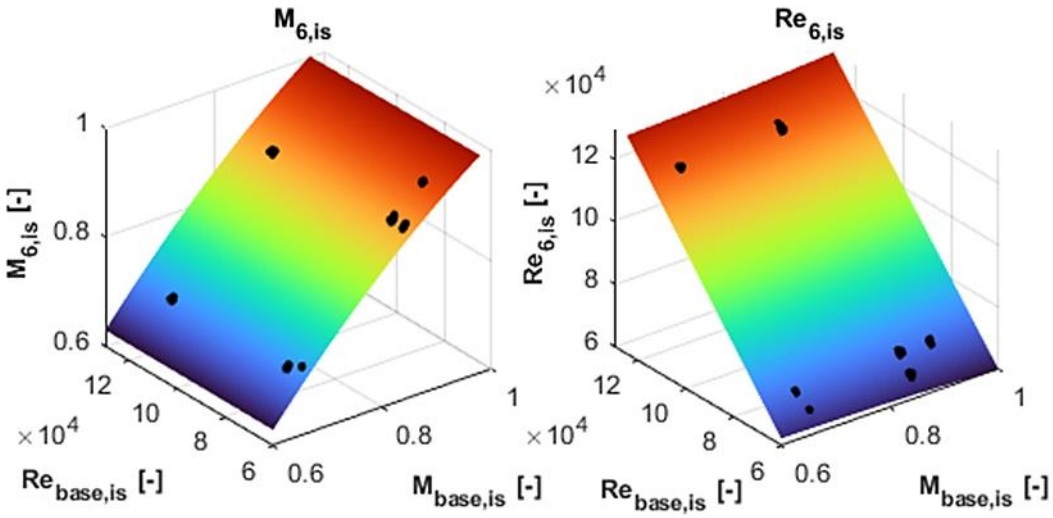

Figure 3.10: Base pressure surface fit for isentropic exit Mach number (left) and isentropic exit Reynolds number (right).

Table 3.6: Coefficients ad R^2 for the $M_{6,is}$ and $Re_{6,is}$ base pressure correlations.

Coefficients	$M_{6,is}$	$Re_{6,is}$
C_1	-0.3448	-6666
C_2	2.026	1.824E+04
C_3	-9.035E-08	1.091
C_4	-0.6689	-1.237E+04
C_5	1.442E-07	-0.07962
R^2	0.9999	1.0000

The isentropic Mach and Reynolds numbers computed with the pressure taps data in Plane 06 are compared against the results of the correlations to assess their quality and usability in retrieving the flow conditions downstream of the cascade.

Figure 3.11 presents the comparison for a typical test without probe in the test section. The base pressure correlation (black dashed line) tracks the evolution of the outlet Mach number (plot at the top) precisely. The computed Reynolds number is slightly underestimated, but the variation is well within the repeatability interval of the flow conditions.

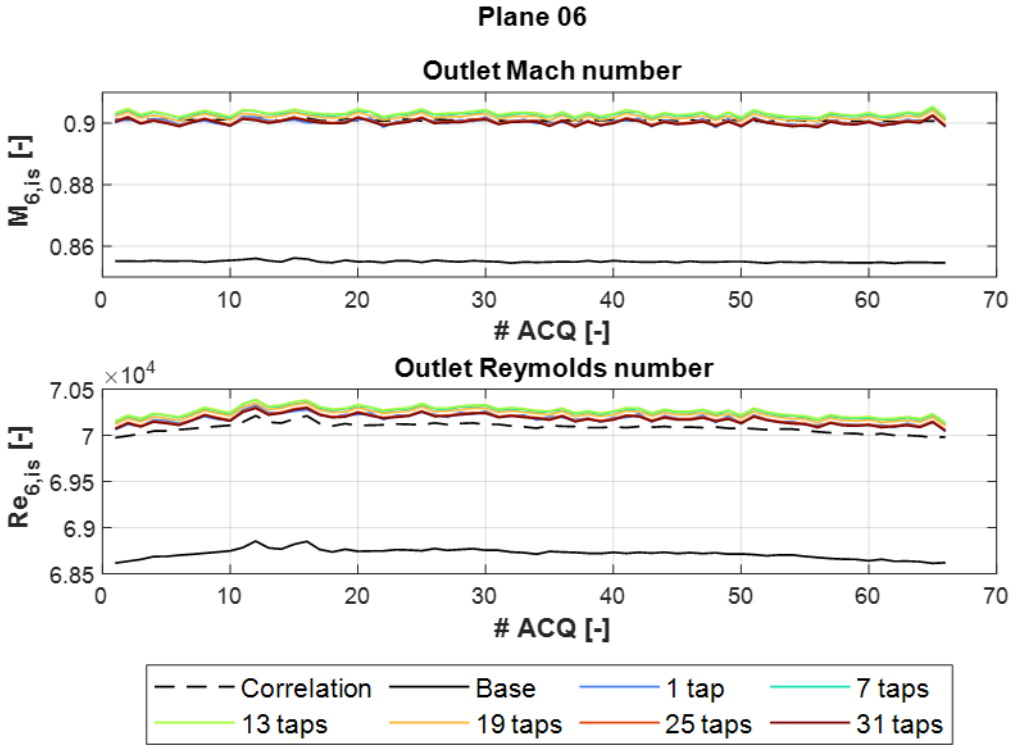

Figure 3.11: Comparison of the evolution of outlet isentropic Mach number (top) and Reynolds number (bottom) computed with the base pressure correlation, base pressure and Plane06 static pressure taps. Test without probe.

The results of the correlation for a test case including probe traverse in Plane 06 is shown in Figure 3.12. The test reported in the figure is the same as the one of Figure 3.8. The Mach and Reynolds number computed with the correlation are higher than the values computed with the pressure taps in Plane 06, independently by how many taps are considered. This is caused by the fact that the correlation was built without the probe in the test section and therefore does not account for pressure losses induced by presence of probe in test section, as the total pressure upstream of cascade is used to compute isentropic quantities at cascade base. Nevertheless, the evolution of the flow conditions is tracked well as demonstrated by the stability of both the Base (black line) and Correlation (black dashed lines) lines in the plots.

Overall, the comparison presented here shows that the use of the base pressure correlation enables to overcome the problem of probe interference while setting and monitoring the operating conditions and can therefore be used during tests which require traversing probes in the test section.

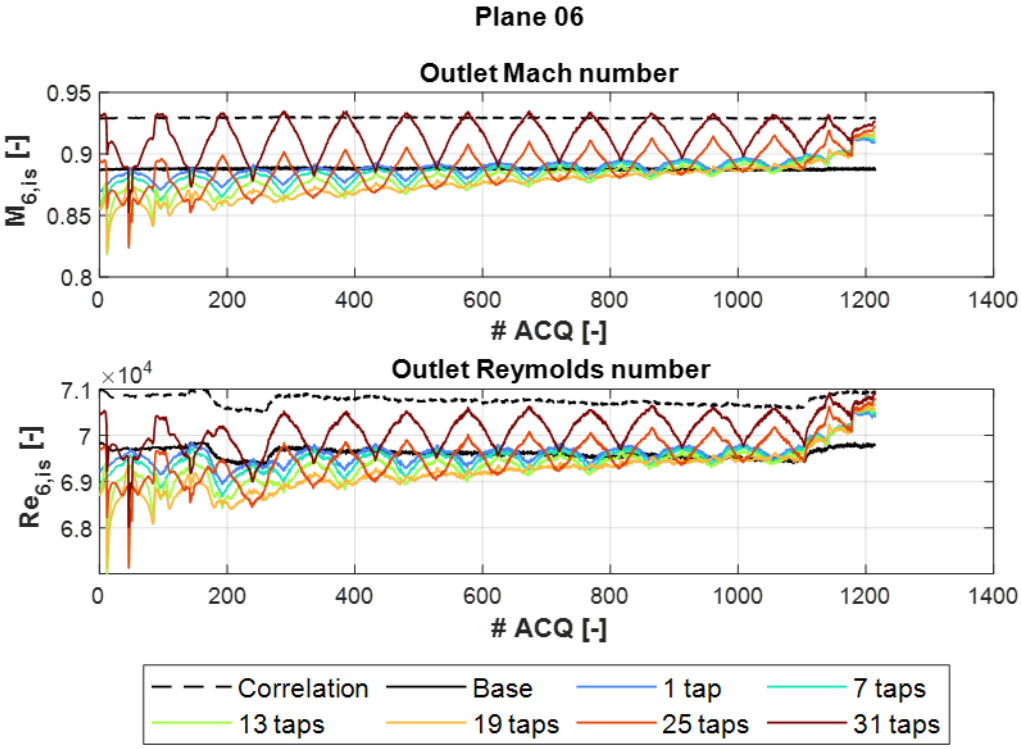

Figure 3.12: Comparison of the evolution of outlet isentropic Mach number (top) and Reynolds number (bottom) computed with the base pressure correlation, base pressure and Plane06 static pressure taps. Test with probe.

4 Data processing

This section aims at providing the definitions of quantities describing the cascade performance (angle, pressures, Mach number, losses) in addition to layout data reduction tools and methods employed for the data post-test treatment.

4.1 Flow angles and pressures from multi-hole probes

4.1.1 Flow angle definitions

The quantities describing the inlet and outlet flow angle are the primary flow direction, β, and the cascade pitch angle, γ. Figure 4.1 displays the positive orientation of the primary flow direction and the cascade pitch angle in the cascade reference system. The primary flow direction can be seen as a projection of the inlet or outlet flow angle on the XY plane. On the other hand, the cascade pitch angle is the projection of the inlet or outlet flow angle on the XZ plane. The primary flow direction , β, and the cascade pitch angle, γ are determined from the flow angles measured by the multi-hole probe to reconcile the reference system of the probe angular calibration and the cascade reference system of Figure 4.1.

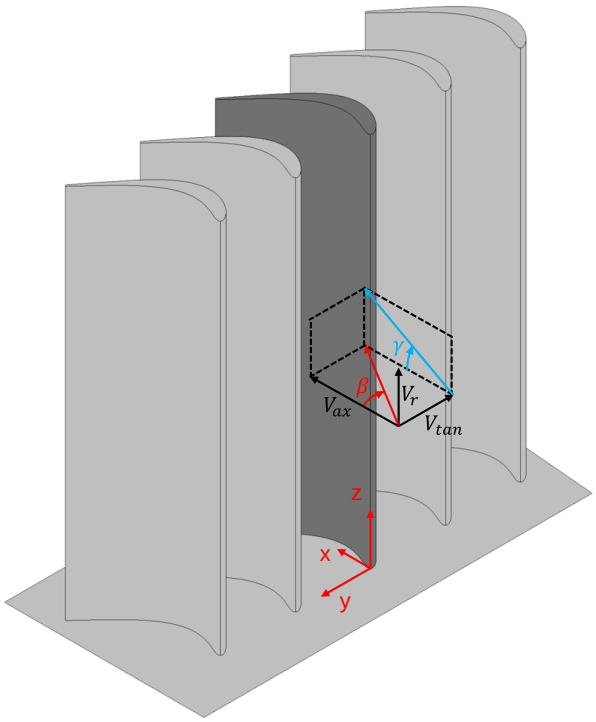

Figure 4.1: Primary flow direction and cascade pitch angle in the cascade reference system

The main quantity used to quantify the outlet flow angle is the primary flow direction

$$\beta = \tan^{-1}\frac{V_{tan}}{V_{ax}}$$

In the case one is interested in the outlet flow under/overturning, the deviation, d, can be computed as $d = \beta - \alpha_{m,outlet}$. Overturning occurs when $d > 0$.
The incidence at the inlet of the cascade, i, can be computed as $i = \beta - \alpha_{m,inlet}$.
The quantity describing the deviation from two-dimensionality is the cascade pitch angle. The latter can be computed as

$$\gamma = \tan^{-1}\frac{V_r}{V_{ax}}$$

4.1.2 Multi-hole probe data reduction

The five-hole probe pressure readings are used to determine the local flow speed, and probe yaw and pitch angles, total pressure and static pressure (or Mach number). The probes are operated in non-nulling mode and are calibrated under atmospheric conditions for a range of yaw (α) and pitch (γ) angles of ±30°, and Mach number between 0.20 and 0.60 (C5HP probe – cascade inlet measurements) and between 0.20 and 0.95 (L5HP probe – cascade outlet measurements).

To retrieve the yaw angle, pitch angle, total pressure, static pressure and Mach number, the following calibration coefficients are calculated:

$$K_{yaw}(\alpha, \gamma, \mathrm{M}) = \frac{P_L - P_R}{P_C - P_{ave}}$$

$$K_{pitch}(\alpha, \gamma, \mathrm{M}) = \frac{P_D - P_U}{P_C - P_{ave}}$$

$$K_{tot}(\alpha, \gamma, \mathrm{M}) = \frac{P_c - P_{tot}}{P_C - P_{ave}}$$

$$K_{stat}(\alpha, \gamma, \mathrm{M}) = \frac{P_{ave} - P_{stat}}{P_C - P_{ave}}$$

$$P_{ave} = \frac{P_L + P_R + P_D + P_U}{4}$$

The local Mach number is retrieved through an iterative process. Due to the finite spatial resolution of the probe ports, measurement errors on the aerodynamic quantities arise. This effect is particularly relevant in flows with high gradients. The first correction proposed by Ligrani et al.[1] to reduce the measurement error is applied to the probe measurement data matrix. The correction procedure consists in interpolating the pressure readings from the five head taps in a single location (chosen here as the probe central tap) to reduce the spatial resolution error.

A non-uniform grid with refinement in the blade wake and endwall region is interrogated by the L5HP probe to resolve the high gradients downstream of the cascade. Wall proximity effects affecting the five-hole probe measurements are avoided by considering data points that are sampled at least two head diameters away from the endwall (H > 4.4 mm) as recommended in [15].

4.2 Cascade AVDR

The axial velocity density ratio (AVDR) is a measure of the two-dimensionality of the flow in the cascade. It can be computed using the following equation

$$AVDR = \int_{\frac{y}{g}=-1}^{\frac{y}{g}=+1} \frac{\rho_{out} V_{ax,out} dy}{\rho_{in} V_{ax,in} dy}$$

Typically, a value of one indicates two-dimensional flow. The computation of the AVDR is performed by means of the quantities derived from the static pressure taps measurements at Plane 01 and 06. The use of this

[1] P. M. Ligrani, L. R. Baun, e B. A. Singer, «Spatial resolution and downwash velocity corrections for multiple-hole pressure probes in complex flows», *Experiments in Fluids*, vol. 7, n. 6, pp. 424–426, 1989.

pressure instead of that from the multi-hole probes reduces the possible errors caused by the probe blockage that is dependent on the Mach number (mainly at the outlet). In addition, the dependency of the probe in retrieving the local static pressure that is needed to compute the Mach number, and therefore local axial velocity is eliminated. The density and velocity are derived from the freestream total pressure and temperature and endwall static pressure assuming that there is no spanwise gradient of static pressure. The flow axial velocity is determined then using the flow angles measured by the five-hole probes upstream and downstream of the cascade at midspan ($V_{ax} = V \cos\beta$).

The AVDR values for the flow conditions where measurements have been performed at Plane 02 with the five-hole probe C5HP and at Plane 06 with the five-hole probe L5HP can be found in "..\Experimental_DataBase\SPLEENC1_TestConditions.xlsx".

4.3 Turbulence

The Hot-Wire probes were operated in constant temperature mode (CTA) using a Dantec Dynamics Streamline Pro anemometer. Prior to each application, the probe frequency response was optimized by a square wave test at the highest observed velocity and was measured to be 10 kHz. Consequently, an analogue low-pass filter at 30 kHz was applied before digitalization by the high-speed 16-bit acquisition card.
The anemometers were operated and processed using the methodology proposed by Cukurel et al.[2]. The method relies on the use of an effective wire temperature and on empirical correlations to remove the reliance of the calibration on the flow total temperature and Mach number, permitting the definition of a unique *Nu* - Re_w calibration curve. The effective wire temperature is the temperature that represents the convective heat transfer from the wire to the flow. A low-speed calibration varying the flow temperature is required to evaluate the effective wire temperature. Once this parameter is known, an in-situ mass-flux calibration can be carried out in the operational velocity and density range typical of the cascade tests. Corrections proposed by Dewey and Klopfer are applied in the high-subsonic regime (M>0.4) and in the low subsonic regime (M<0.4) to correct the Nusselt number from Mach effects. In the data processing phase, an iterative loop is applied to compute the corrected Nusselt number based on the local flow conditions and determine the wire Reynolds, and thus the flow velocity, through the mass-flux calibration.

The cascade inlet turbulence is characterized in terms of free stream turbulence intensity (FSTI) and an integral length scale (ILS).
The computation of the free steam turbulence intensity is based on the sensitivity coefficients method reported in the works of Cukurel et al. and Boufidi and Fontaneto[3]. The assumption that the fluctuations of density and temperature are negligible is made to allow the computation of the turbulent velocity fluctuations with a single wire. Consequently, the fluctuations of velocity, and therefore the turbulence intensity can be retrieved from the following equation:

$$TI\ [\%] = 100 * \frac{1}{S_V} \cdot \frac{E'}{\bar{E}}$$

The measured average turbulence intensity downstream of the turbulence grid (no wake generator installed) is close to design target of 2.5%. Moreover, the pitchwise distribution shows a variation associated with the turbulence decay due to the relative inclination of the cascade and the turbulence grid. While traversing the probe across the two central passages from pitch = + 1 to pitch y/g = - 1, the axial distance between the probe and the turbulence grid reduces by 48 mm and results in a continuous increase of measured turbulence intensity. The measured turbulence intensity decay provides a measure of the turbulence dissipation rate.

The integral length scale Λ_x is considered a measure of the largest eddy size in a turbulent flow and in this work is calculated using the method proposed in Roach et al.[4]. The turbulence integral length scales are

[2] B. Cukurel, S. Acarer and T. Arts, "A Novel Perspective to High-Speed Cross-Hot-Wire Calibration Methodology," Experiments in Fluids, vol. 53, no. 4, pp. 1073-1085, 2012.
[3] E. Boufidi and F. Fontaneto, "Towards a more reliable application of hot-wire anemometry in complex compressible flows," in XXIII Biannual Symposium on Measuring Techniques in Turbomachinery, Transonic and Supersonic Flow in Cascades and Turbomachines, Stuttgart, Germany, 2016.
[4] P. E. Roach, "The generation of nearly isotropic turbulence by means of grids," International Journal of Heat and Fluid Flow, vol. 8, no. 2, pp. 82-92, 1987.

computed from the Power Spectral Density function (PSD) of the wire voltage signal, assuming truly uniform and isotropic turbulence:

$$\Lambda_x = \cdot \bar{V} \cdot \left[\frac{E(f)}{4\overline{V'^2}}\right]_{f\to 0}$$

Where Λ_x is the integral length scale based on a one-component velocity signal. To compute $[E(f)]_{f\to 0}$ the power spectrum is averaged up to the frequency before the decay, determined to be 100 Hz. The measured value of integral length scale (also indicated as ILS) downstream of the turbulence grid (no wake generator installed) is close to the turbulence grid spacing of 12 mm.

4.4 Energy loss coefficient

There are multiple ways to assess the loss coefficient in turbines. For the case of a stationary row of blades where the flow expands adiabatically and no work is exchanged, the loss generation can be related to entropy generation.[5] The energy loss coefficient is less sensitive to Mach number than the total pressure and entropy loss coefficients[6]. For these reasons, the energy loss coefficient, ξ, used in this investigation is defined as:

$$\xi = 1 - \frac{1 - \left(\frac{P_6}{P_{06}}\right)^{\frac{\gamma-1}{\gamma}}}{1 - \left(\frac{P_6}{P_{01,fs}}\right)^{\frac{\gamma-1}{\gamma}}}$$

In the above equation, the total pressure P_{06}, and the static pressure P_6 are those measured downstream of the cascade by the five-hole probe L5HP, while the freestream inlet total pressure, $P_{01,fs}$, is measured upstream of the cascade, and downstream of the turbulence grid (for test without wake generator) or in Plane 02 when the wake generator is installed. The inlet total pressure is a single value computed with the loss coefficient correlation (sections 3.2 and 3.3). Hereby is recalled that the inlet total pressure value used to build the inlet TG loss correlations results from pitchwise area-averaging the total pressure distribution at midspan over ± 1 cascade pitch.

4.5 Quasi-shear stress

The surface mounted hot-films operation is based on the relation between the convective heat flux, Q, and shear stress, τ_w:

$$\tau_w = \left(\frac{Q}{\Delta T \cdot k}\right)^3$$

To obtain absolute values of the shear stress, an extensive calibration of the sensors under a controlled environment for a known boundary layer is required. This calibration is extremely elaborated, prone to errors and was not performed in this experimental study. Therefore, only a qualitative description of the wall shear is determined from hot-film measurements: the quasi-wall shear stress, τ_q, efined as:

$$\tau_q = \left(\frac{Q - Q_0}{Q_0}\right)^3$$

Where Q is the total dissipated power by each sensor with flow and Q_0 is the total dissipated power without flow. This definition can be employed as long as the driving temperature between the flow and the hot sensor

[5] Denton, J. D. (1993). Loss mechanisms in turbomachines (Vol. 78897, p. V002T14A001). American Society of Mechanical Engineers.
[6] Brown, L. E. (1972). Axial flow compressor and turbine loss coefficients: A comparison of several parameters.

is the same under flow and no-flow regimes. As the sensors are operated at constant temperature, the previous equation can be expressed as:

$$\tau_q \approx \left(\frac{E^2 - E_0^2}{E_0^2}\right)^3$$

Where E is the bridge voltage with flow and E_0 is the bridge voltage without flow. The E_0 must be acquired for the same temperature difference established between the hot sensor and flow to reduce the impact of small differences in the sensor properties. A correction[7] to the measured voltage is applied to compensate the increase of flow temperature and blade metal temperature occurring during a typical testing day, whereas the sensor temperature remains constant as imposed by the anemometer.
The acquired voltage is corrected according to the formula below:

$$E_{corr} = E \times \sqrt{\frac{T_w - T_{ref}}{T_w - T_{0,test}}}$$

Where T_w is the hot sensor temperature, T_{ref} is the reference temperature at which the bridge was setup and $T_{0,test}$ is the total temperature inside the test section during the test. This correction is applied to the voltage with and without flow. The quasi-wall shear stress has been computed using the no-flow sensor voltage offset E_0 taken right after the end of a test day at a pressure level close to that of the static pressure during the flow-on phase (P ~ 7,000 – 10,000 Pa).
All the acquired hot-film signals on both blade and cascade endwall were digitally low-pass filtered at a cut-off frequency of 8 kHz. For tests performed with the wake generator, hot-film signals were filtered at 30 kHz.

4.6 Averaging methods

The average procedure is dependent on the context of evaluation and the intended purpose.

4.6.1 Area-averaging

Area-averaging is typically employed to average the static pressure field. The mathematical definitions of a generic quantity, Φ, area-averaged over the pitchwise direction, as well as over the pitch and spanwise directions (planewise averaged) are as follow

$$\text{pitchwise}, \Phi^a = \frac{1}{g}\int_{-g}^{g} \Phi(y)dy$$

$$\text{planewise}, \Phi^a = \frac{1}{gH}\int_{0}^{H}\int_{-g}^{g} \Phi(y,z)dydz$$

In addition, area-averaging is sufficient to satisfy the mass equation. Therefore, can also be used for velocity fields, and therefore flow angle fields. Even though the latter quantities are computed by means of the stagnation pressure, the difference between area- and mass-averaged flow angles is lower than 0.10°.

4.6.2 Mass-averaging

The mass-averaging procedure allows to account for mass deficit in boundary and/or shear layers as a reduction in the enthalpy flux instead of a direct loss. This becomes useful when a loss definition derived from enthalpy conservation is used. Consequently, this procedure is recommended for averaging total temperatures and total pressures. The mathematical definitions of a generic quantity, Φ, mass-averaged over the pitchwise direction, and over the pitch and spanwise directions (planewise averaged) are as follow

[7] M. a. S. A. J. Hultmark, "Temperature corrections for constant temperature and constant current hot-wire anemometers," Measurement Science and Technology, vol. 21, no. 10, p. 105404, 2010

$$\text{pitchwise}, \Phi^m = \frac{\frac{1}{g}\int_{-g}^{g} \rho(y) V_{ax}(y) \Phi(y) dy}{\frac{1}{g}\int_{-g}^{g} \rho(y) V_{ax}(y) \Phi dy}$$

$$\text{planewise}, \Phi^m = \frac{\frac{1}{gH}\int_{0}^{H}\int_{-g}^{g} \rho(y,z) V_{ax}(y,z) \Phi(y,z) dydz}{\frac{1}{gH}\int_{0}^{H}\int_{-g}^{g} \rho(y,z) V_{ax}(y,z) \Phi dydz}$$

4.6.3 Combination of quantities

In the case a quantity is computed by combining static and total quantities, each one of the quantities constituting the final quantity are averaged according to the sections 4.6.1 and 4.6.2. This is the case for the kinetic energy loss coefficient used to characterize the cascade losses. The mass-averaged energy loss coefficient is computed as follows

$$\xi^m = 1 - \frac{1 - \left(\frac{P_6^a}{P_{06}^m}\right)^{\frac{\gamma-1}{\gamma}}}{1 - \left(\frac{P_6^a}{P_{01}^m}\right)^{\frac{\gamma-1}{\gamma}}}$$

4.6.4 Phase-Locked (ensemble) averaging

The phase locked average (PLA) technique has been used to extract the time-resolved fluctuations periodic with the bar passing frequency from fast-response instrumentation.
For a periodic quantity $\Phi(t)$, the method consists in averaging the signals over several repeating periods, N_{per}. Each period is discretized in several classes, N_{class}, that discretize the period of the repeating event into smaller portions. The original signal is broken down into repeating events, and points belonging to the same class are averaged to obtain the final ensemble-average signal. The PLA method can be defined mathematically by the following equation:

$$\widetilde{\Phi}(t_i) = \frac{1}{N_{per}} \sum_{j=1}^{N_{per}} \Phi_j(t_i), \qquad i = 1 \ldots N_{class}$$

The fluctuations in each class can be estimated as

$$\Phi'(t_i) = \frac{1}{N_{per}} \sum_{j=1}^{N_{per}} \left(\Phi_j(t_i) - \widetilde{\Phi}(t_i)\right), \qquad i = 1 \ldots N_{class}$$

Lastly, the RMS of each class can be estimated by

$$RMS(t_i) = \sqrt{\Phi'^2(t_i)}, \qquad i = 1 \ldots N_{class}$$

Note that the latter is equivalent to computing the standard deviation of $\Phi_j(t_i)$.

In the scope of this project, the higher order statistical moments (see section 4.6.4 for skewness and kurtosis) of the fluctuations in each class are also determined and reported. The definitions of statistical moments found in section 4.6.4 are applied to each class composing the ensemble-averaged signal.

Figure 4.2 provides a visual interpretation of the above equations. Figure 4.2 (top) displays the calibrated pressure signal measured by the fast response Kulite sensor #4 present on the blade SS. The signal was acquired

during measurements performed at midspan for the case of $M_{6,is} = 0.95$; $Re_{6,is} = 70k$. This flow condition will be used for the explanatory purpose of this section.
The signal can be broken down in every WG disk revolution, which in this case is periodic. The repeated signals can then be rephased with a triggering event (1st wake generator bar) to be averaged and reduced the measurement random error. Figure 4.2 (bottom) displays the rephased repeating signals in one WG disk revolution period featuring 96 bar passing events.

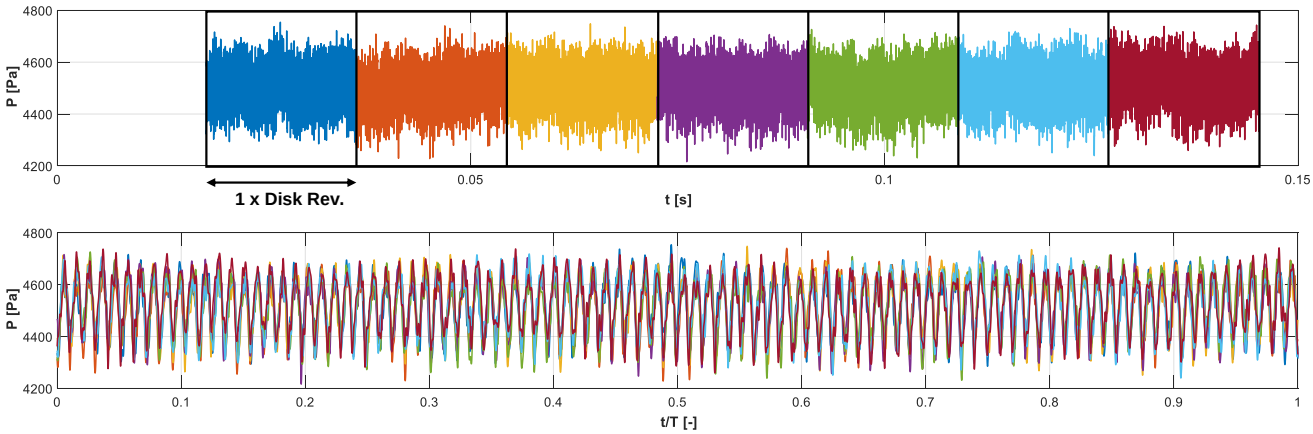

Figure 4.2: Breakdown of WG disk revolutions into periodic events (top) and rephasing of the WG repeating events over one disk revolution period (bottom)

The repeating event can be one bar passing or the entire disk revolution (i.e., 96 bar passing events). Averaging over one single bar passing period further increases the number of existing events to be averaged. For this to be possible, all bars must be similar. To assess this assumption, the PLA of a signal averaged over one disk revolution has been compared with the PLA of a signal averaged for one bar passing and multiplied by 96 events. It is reasonable to assume that if the bars are identical, they generate repeatable wakes with wake-induced flow fluctuations that are also periodic and repeatable.

Figure 4.3 (top) displays the back-to-back comparison of the normalized pressure measured by the 4th fast-response Kulite pressure sensor on the blade SS, averaged over a disk revolution against the same signal averaged over a bar passing period and repeated 96 times. From a visual inspection alone, the signals seem to overlap. The difference in the ensemble average periodic signal obtained through the two approaches is displayed in Figure 4.3 (bottom). The maximum difference between the two cases is found to be ~$0.005P_{01}$ (~50 Pa). The standard deviation of their difference over a disc revolution is ~$0.0016P_{01}$ (~15 Pa). For the scope of this database, in view of the high repeatability of the bar wakes, only the periodic signals averaged over the bar passing event are reported.

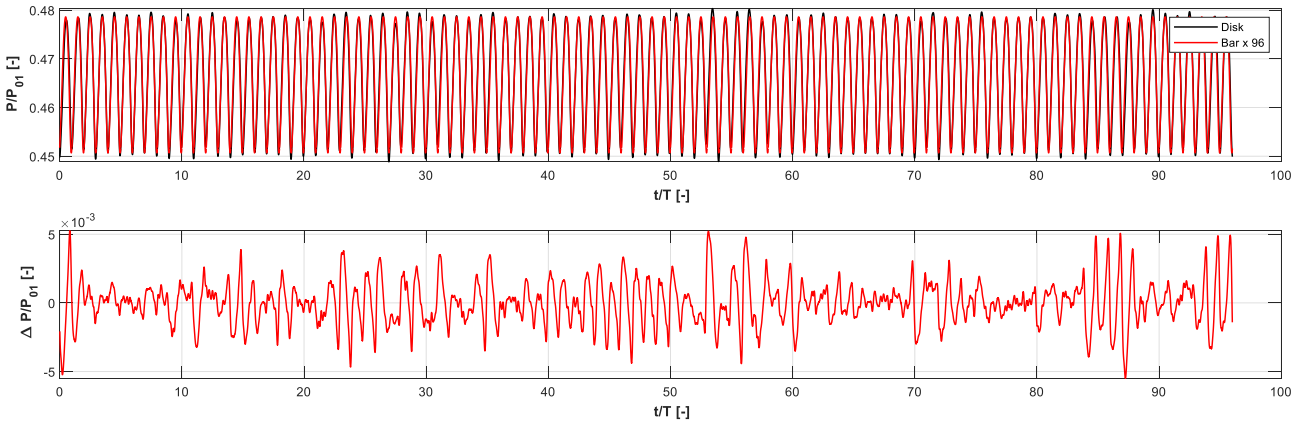

Figure 4.3: Comparison of PLA a signal averaged for one disk revolution vs. one bar passing multiplied by the number of bars in the disk (top) and error from assuming similarity between each bar (bottom)

The bar passing period is discretized with 227 classes, such that there is at least one point per class at the given sampling frequency and bar passing frequency ($N_{class,opt} = F_s/F_{bar}$).

The impact of reducing the number of classes to house more points per class is displayed in Figure 4.4. This figure displays the difference between ensemble-averaged signals with different number of classes against the ensemble-averaged signal with the optimal number of classes (227). As the number of classes is increased above 75, there is virtually no variation of the ensemble-averaged signal.
Eventually, 227 classes have been used to determine the ensemble-averaged periodic component from all time-accurate measurements acquired under the presence of incoming periodic wakes.

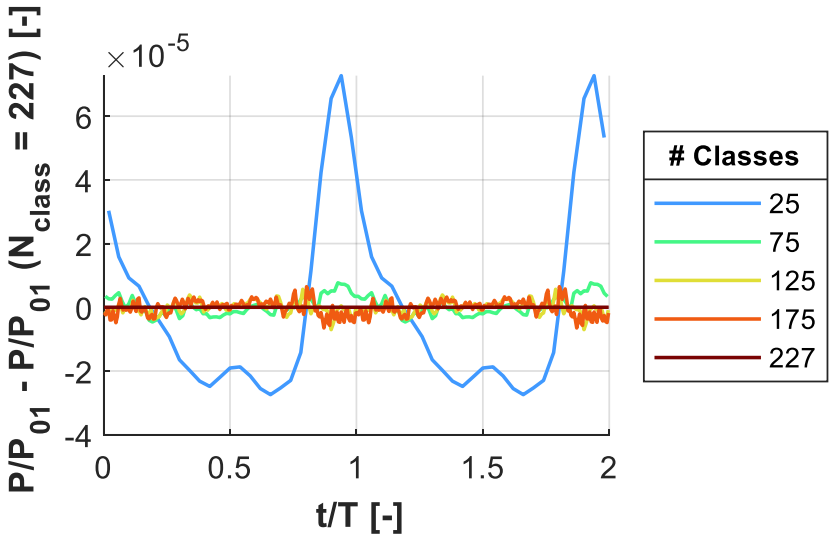

Figure 4.4: Impact of reducing the number of points/per class on PLA signal error

The number of averaging a different number of bar passing events has also been addressed in the scope of this work. This was accomplished by studying the evolution of the PLA signal as more repeating events are added to the average. For typical acquisitions of time-accurate measurements, around 15, 000 events occur during a sampling time of 3 s. Figure 4.5 (left) displays the evolution of the PLA signal over one bar passing period as the number of averaged events increases. The difference between the PLA using the maximum number of events and the PLA using increasing number of events is displayed in Figure 4.5 (right). The ensemble-average signal remains is statistically converged already after two hundreds bar passing events. The maximum number of available events is always used to perform the ensemble-average of all acquired signals. The error induced by averaging over a finite signal duration is therefore considered negligible for instantaneous pressure and shear-stress measurements.

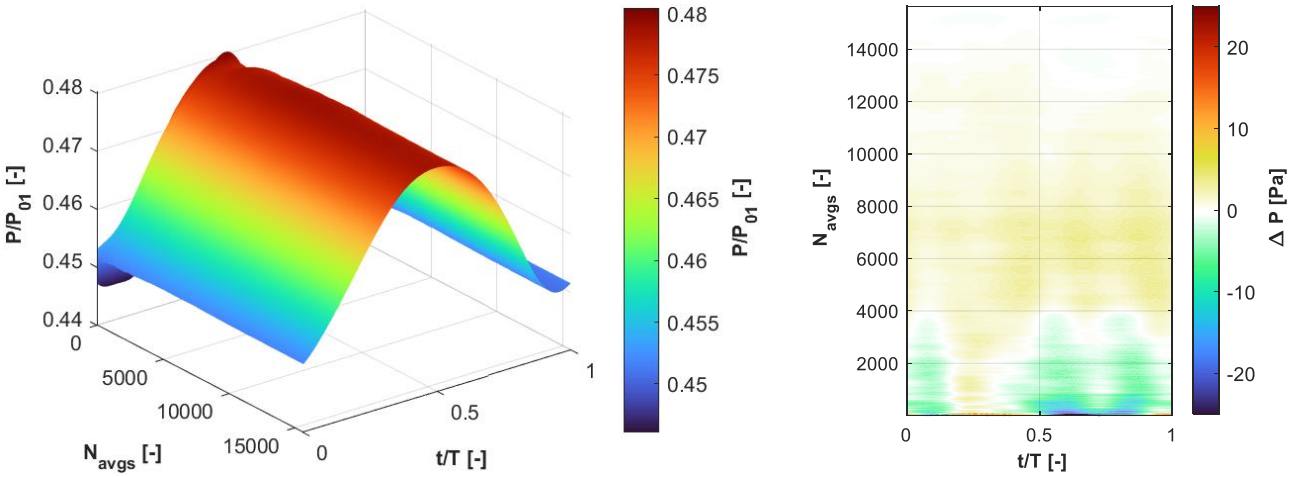

Figure 4.5: Evolution of a PLA signal as a function of the number of averaged events (left) and difference between the PLA performed with the maximum number of events and the PLA performed with increasing number of events over one bar passing period (right)

The signal of each bar passing event is compared against the final ensemble-averaged signal in Figure 4.6 (left). For each class, the scattered points from the 15,648 bar passing events have been verified to follow a Gaussian distribution as suggested in Figure 4.6 (right) for the class #40.

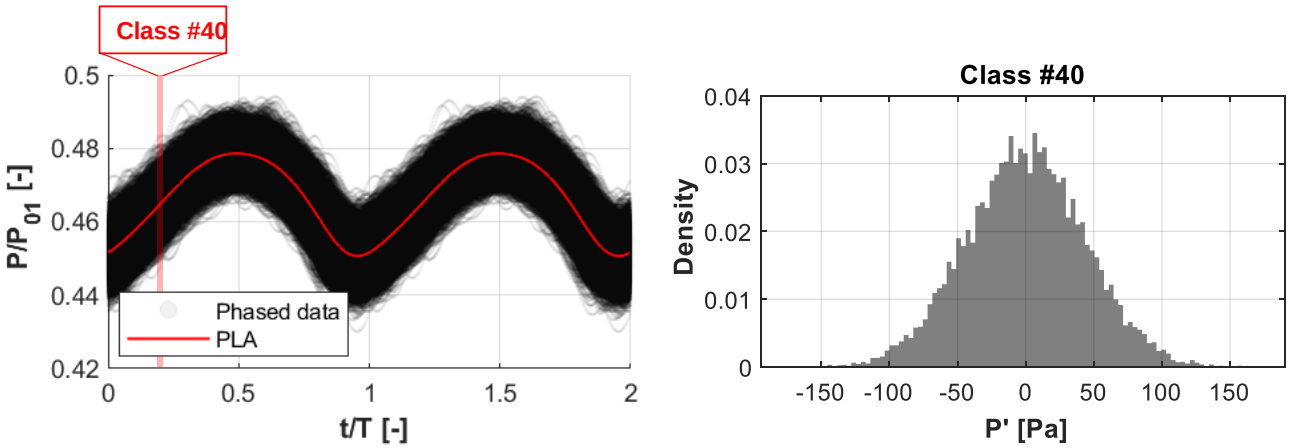

Figure 4.6: Rephased points for two bar passing periods along the PLA (left) and histogram describing normal distribution of set of points belonging to class #40 (right)

4.7 Statistical moments

The raw/calibrated signals obtained during tests performed with fast-response instrumentation are often characterized by means of their statistical moments. The definitions of the used statistical moments for a generic quantity $\Phi(t)$ are recalled below.
The standard deviation used in the scope of this work is defined as:

$$std(\Phi(t)) = \sqrt{\frac{1}{N-1}\sum_{t=1}^{N}|\Phi(t) - \bar{\Phi}|^2}$$

Where $\bar{\Phi}$ is the time-mean of $\Phi(t)$ and N is the number of samples of the signal.
The skewness is defined as:

$$skew(\Phi(t)) = \frac{\frac{1}{n}\sum_{t=1}^{N}(\Phi(t) - \bar{\Phi})^3}{\left(\sqrt{\frac{1}{n}\sum_{t=1}^{N}(\Phi(t) - \bar{\Phi})^2}\right)^3}$$

The kurtosis is defined as:

$$kurt(\Phi(t)) = \frac{\frac{1}{n}\sum_{t=1}^{N}(\Phi(t) - \bar{\Phi})^4}{\left(\frac{1}{n}\sum_{t=1}^{N}(\Phi(t) - \bar{\Phi})^2\right)^2}$$

5 Uncertainty

5.1 Definitions and error propagation

The measurement uncertainty is evaluated by the ASME Measurement Uncertainty method[8].

The errors have been categorized as "random" for errors that varied during the measurement period and as "systematic" for errors that were invariant during the measurement period.

The combined total uncertainty of a measured quantity can be estimated as:

$$\delta\Phi = \sqrt{\Phi_{sys}^2 + \Phi_{rand}^2}$$

In the following, all values of uncertainty have been computed and reported with a 95% confidence level.
Then, for a generic quantity q depending on independent parameters $\Phi_1, \Phi_2, \Phi_3, \dots, \Phi_n$:

$$q = f(\Phi_1, \Phi_2, \Phi_3, \dots, \Phi_n)$$

The uncertainty propagation into the derived quantity q of all the uncertainty terms is determined through a Taylor Series Method (TSM) with higher-order terms neglected.
For small variations of the parameter Φ_i, the effect of the associated uncertainty $\delta\Phi_i$ on the propagated uncertainty δq can be expressed in linear form:

$$\delta q = \sqrt{\sum_{i=1}^{n} \left(\frac{\partial \mathrm{q}}{\partial \Phi_i}\delta\Phi_i\right)^2}$$

Where the term $\partial q / \partial \Phi_i$ is the sensitivity coefficient expressing the dependence of q on Φ_i.

[8] *R. B. Abernethy, R. P. Benedict, and R. B. Dowdell. ASME Measurement Uncertainty. Journal of Fluids Engineering, 107(2):161, 1985.*

5.2 Measurement uncertainties

The systematic, random, and overall uncertainties with 95% confidence interval contained are reported in Table 5.1 for all measured quantities included in this database.
The uncertainties reported in the table show that systematic terms are generally the largest contributors to the overall measurement uncertainty.
As a general consideration, the difference between the same measurement performed at different operating points (in terms of cascade operating exit Mach number and Reynolds number), and/or pitch and span locations, is not markedly affected by systematic errors, being the quantities measured by the same calibrated transducers and measurement chains over relatively unchanged experimental setups[9]. For these reasons, the uncertainty on the difference between such measurements is argued to be dominated by the random error terms, with extremely small systematic uncertainty.

[9] H. W. Coleman and W. G. Steele, Experimentation, Validation, and Uncertainty analysis for Engineers, Hoboken, USA: 8 John Wiley & Sons, Inc., 2018.

Table 5.1: Measurement uncertainty

			Uncertainty (95% confidence interval)		
Quantity	**Symbol**	**Unit**	**Random**	**Systematic**	**Total**
Fixed instrumentation/Blade/Endwalls/Op. conditions					
Inlet total temperature	Tref	K	0.002	0.516	0.516
Static pressure	P	Pa	1.0	28.6	28.6
Cascade Isentropic exit Mach number	M2,is	-	0.0007	0.0054	0.0054
Static temperature	T	K	0.056	0.624	0.626
Density	ρ	kg m^-3	2.1E-05	4.2E-04	4.2E-04
Velocity	v	m s^-1	0.2	1.8	1.8
Blade chord	C	mm	0.00	0.05	0.05
Dynamic viscosity	μ	kg m^-1 s^-1	2.8E-09	3.1E-08	3.2E-08
Cascade Isentropic exit Reynolds number	Re2,is	-	59	881	883
WG rotational speed	Omega	RPM	0.003	0.098	0.098
WG Strouhal number	St	-	0.001	0.010	0.011
WG bar phase	t/T	-	0.004	0.003	0.005
Axial velocity density ratio	AVDR	-	0.003	0.023	0.023
Blade - Fast-Response pressure					
Static pressure	P	Pa	0.1	43.2	43.2
Isentropic Mach number	M6,is	-	0.0000	0.0082	0.0082
Endwall - Fast-Response pressure					
Static pressure	P	Pa	0.1	46.0	46.0
Isentropic Mach number	M6,is	-	0.0000	0.0087	0.0087
Probe positioning					
Linear position	x, y, z	mm	0.00	0.10	0.10
Angular position (yaw)	α_{set}	deg	0.00	0.1000	0.100
Boundary layer probe					
Total pressure	P_{BL}	Pa	1.0	25.4	25.4
PBL over P01	P_{BL} / P_{01}	-	0.0007	0.0040	0.0041
PBL over P1stat	P_{BL} / P_{1stat}	-	0.0002	0.0054	0.0054
Cobra 5HP					
Total pressure	P02	Pa	5.6	26.7	27.3
Static pressure	P2	Pa	5.6	21.0	21.7
(Probe) Yaw angle	α	deg	0.20	1.02	1.04
(Probe) Pitch angle	γ	deg	0.20	0.58	0.61
Mach number	M2	-	0.002	0.006	0.006
L-shaped 5HP					
Total pressure	P06	Pa	6.0	26.0	26.7
Static pressure	P6	Pa	6.0	16.8	17.8
(Probe) Yaw angle	α	deg	0.20	0.22	0.29
(Probe) Pitch angle	γ	deg	0.20	0.20	0.28
Mach number	M6	-	0.0014	0.0037	0.0040
Hot-wire anemometry					
Velocity	u	%mean	0.002%	2.33%	2.33%
Turbulence intensity	TI	%u	-	0.10%	0.10%
Integral length scale	ILS	mm	-	2.0	2.0
Derived Quantities					
TG & WG pressure loss coefficient	Ytot	-	0.0007	0.0017	0.0019
Inlet total pressure - Correlation	P01	Pa	7.1	29.8	30.7
Inlet Primary flow direction	βin	deg	0.15	0.77	0.78
Outlet Primary flow direction	βout	deg	0.14	0.18	0.23
Inlet incidence	*i*	deg	0.18	0.77	0.79
Outlet angle deviation from flow direction	*d*	deg	0.17	0.20	0.27
P02 over P01	P_{02} / P_{01}	-	0.0010	0.0041	0.0042
P2stat over P01	P_{2stat} / P_{01}	-	0.0009	0.0033	0.0035
P06 over P01	P_{06} / P_{01}	-	0.0009	0.0040	0.0041
P6stat over P01	P_{6stat} / P_{01}	-	0.0007	0.0025	0.0026
Kinetic energy loss coefficient	ξ	-	0.0019	0.0081	0.0083

6 List of related publications (up to October 30th, 2022)

L. Simonassi, G. Lopes, S. Gendebien, A. F. M. Torre, M. Patinios, S. Lavagnoli, N. Zeller, L. Pintat, "An Experimental Test Case for Transonic Low-Pressure Turbines - Part 1: Rig Design, Instrumentation and Experimental Methodology," In ASME Turbo Expo 2022: Turbine Technical Conference and Exposition. The American Society of Mechanical Engineers (ASME). GT2022-81566, V10BT30A012; 14 pages https://doi.org/10.1115/GT2022-81566

G. Lopes, L. Simonassi, A. F. M. Torre, M. Patinios, and S. Lavagnoli, "An Experimental Test Case for Transonic Low-Pressure Turbines - Part 2: Cascade Aerodynamics at On- and Off- Design Reynolds and Mach Numbers," In ASME Turbo Expo 2022: Turbine Technical Conference and Exposition (pp. GT2022-82626). The American Society of Mechanical Engineers (ASME). GT2022-82626; V10BT30A027 https://doi.org/10.1115/GT2022-82626

A. F. M. Torre, M. Patinios, G. Lopes, L. Simonassi, and S. Lavagnoli, "Vane-Probe Interactions in Transonic Flows," In ASME Turbo Expo 2022: Turbine Technical Conference and Exposition (pp. GT2022-82549). The American Society of Mechanical Engineers (ASME). GT2022-82549; V10BT30A027 https://doi.org/10.1115/GT2022-82549

G. Lopes, L. Simonassi, and S. Lavagnoli, "Instrumentation Interference in a Transonic Linear Cascade" In Conference proceedings of XXVI Biennial Measuring Techniques in Turbomachinery Transonic and Supersonic Flow in Cascades and Turbomachines. Paper MTT2622absA25